iScience

CellPress

Article

N-Doped Mo_2C Nanobelts/Graphene Nanosheets Bonded with Hydroxy Nanocellulose as Flexible and Editable Electrode for Hydrogen Evolution Reaction

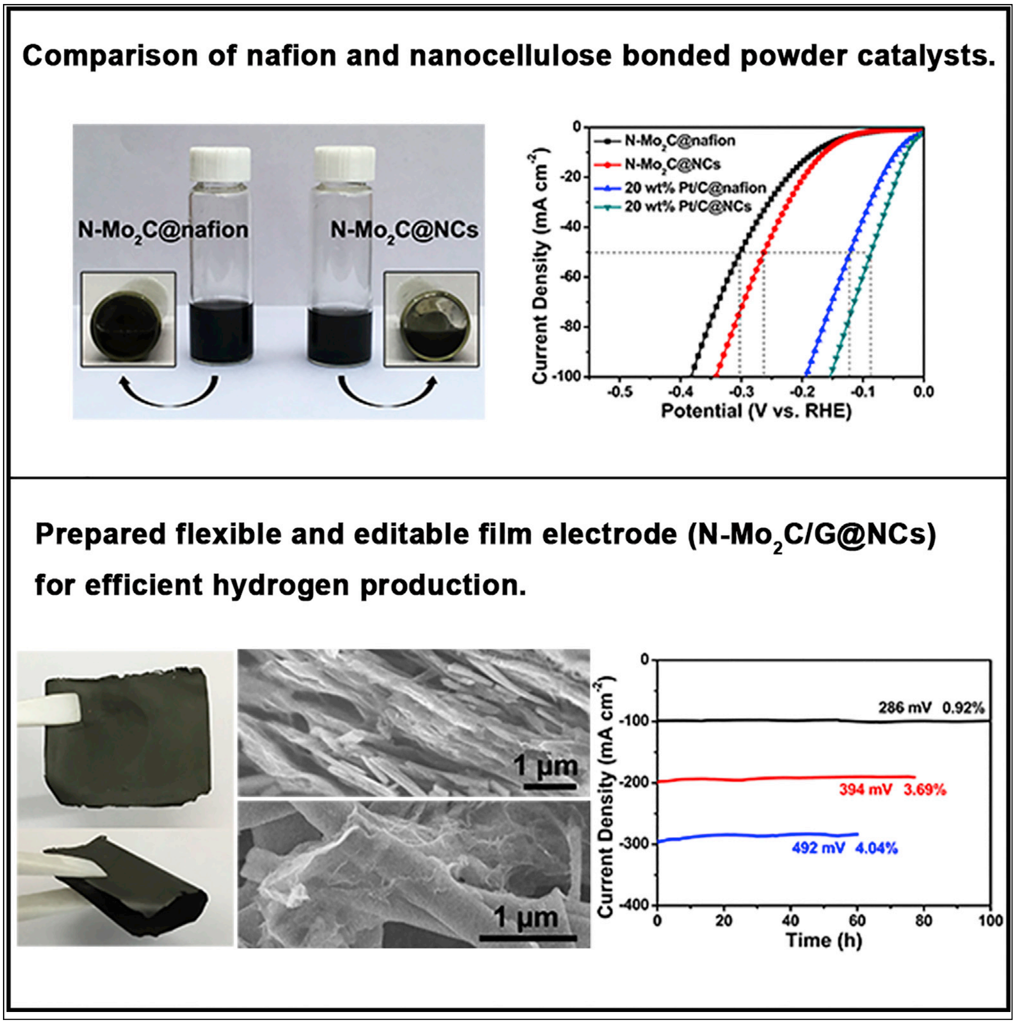

Guixiang Li,
Jiayuan Yu, Ziqian
Zhou, ..., Xinwen
Peng, Hong Liu,
Weijia Zhou

hongliu@sdu.edu.cn (H.L.)
ifc_zhouwj@ujn.edu.cn (W.Z.)

HIGHLIGHTS

N-Mo_2C nanobelts with porous structure are uniformly synthesized

Nanocellulose is proposed to replace Nafion for binding powder catalysts

A facile strategy to prepare conductive film electrode is offered with practice

The flexible editable electrode exhibits excellent performance for scalable HER

Li et al., iScience *19*, 1090–1100
September 27, 2019 © 2019 The Author(s).
https://doi.org/10.1016/j.isci.2019.08.055

iScience

CellPress

Article

N-Doped Mo_2C Nanobelts/Graphene Nanosheets Bonded with Hydroxy Nanocellulose as Flexible and Editable Electrode for Hydrogen Evolution Reaction

Guixiang Li,[1,2,5] Jiayuan Yu,[2,5] Ziqian Zhou,[2,5] Renkun Li,[3] Zhihua Xiang,[3] Qing Cao,[2] Lili Zhao,[1] Xiwen Wang,[3] Xinwen Peng,[3] Hong Liu,[1,4,6,*] and Weijia Zhou[1,2,*]

SUMMARY

The large-scale application of economically efficient electrocatalysts for hydrogen evolution reaction (HER) is limited in view of the high cost of polymer binders (Nafion) for immobilizing of powder catalysts. In this work, nitrogen-doped molybdenum carbide nanobelts (N-Mo_2C NBs) with porous structure are synthesized through a direct pyrolysis process using the pre-prepared molybdenum oxide nanobelts (MoO_3 NBs). Nanocellulose instead of Nafion-bonded N-Mo_2C NBs (N-Mo_2C@NCs) exhibits superior performance toward HER, because of excellent dispersibility and multiple exposed catalytically active sites. Furthermore, the conductive film composed of N-Mo_2C NBs, graphene nanosheets, and nanocellulose (N-Mo_2C/G@NCs) is fabricated by simple vacuum filtration, as flexible and editable electrode, which possesses excellent performance for scale HER applications. This work not only proposes the potential of nanocellulose to replace Nafion for binding powder catalysts, but also offers a facile strategy to prepare flexible and conductive films for a wide variety of nanomaterials.

INTRODUCTION

With the depletion of energy sources (such as oil and coal) and the environmental problems caused by burning fossil fuels (global warming, air and water pollution, etc.), green renewable energy sources such as solar energy and hydrogen energy are bound to become an important energy source for future development (Gray, 2009; Turner, 2004; Hui et al., 2019). Hydrogen energy is an extremely superior new energy source with high combustion heat value, no pollution, rich resources, and wide application range, which is regarded as the ideal clean energy in the future (Dresselhaus and Thomas, 2001; Yu et al., 2018a, 2018b). Among various hydrogen production procedures, electrochemical water splitting is inherently considered to be an ideal eco-friendly method to produce hydrogen with high purity (Koper, 2013; Walter et al., 2010; Zeng et al., 2018; Yu et al., 2019). Efficient water splitting typically requires highly active electrocatalysts to promote the hydrogen evolution reaction (HER) (Huang et al., 2018; Fang et al., 2019). Recently, tremendous efforts have been devoted to search for non-precious metal catalysts to replace Platinum (Pt)-based catalysts in the hydrogen generation with high current densities at low overpotentials, which is thus highly desirable (Wang et al., 2016; Shi and Zhang, 2016; Voiry et al., 2016). In particular, as an alternative, molybdenum-based catalysts, such as molybdenum disulfide (MoS_2) (Geng et al., 2016), molybdenum diselenide ($MoSe_2$) (Deng et al., 2018), molybdenum phosphide (MoP) (Xiao et al., 2014), molybdenum carbide (Mo_2C) (Humagain et al., 2018), and molybdenum nitride (MoN) (Zhang et al., 2016), have recently attracted great attention as potential catalysts for HER, owing to their high cost-effectiveness, abundant molybdenum resources, favorable catalytic activities, and excellent stabilities (Xing et al., 2014; Vrubel and Hu, 2012; Xie et al., 2014). Among them, Mo_2C, an excellent transition metal carbide, has received increasing attention as a highly efficient HER electrocatalyst with high conductivity and optimal hydrogen absorption energy, in view of the fact that its electronic structure is almost identical to that of Pt-group elements (Wu et al., 2015; Zhao et al., 2015; Wan et al., 2014). To date, several kinds of Mo_2C nanostructures have been successfully synthesized and showed the enhanced performance for HER (Wu et al., 2015; Yang et al., 2016; Xu et al., 2016). It is well known that the electrocatalytic properties of metal carbides strongly depend on their surface structure and composition, which are closely associated with the porous structure and element doping (Wu et al., 2015; Wang et al., 2015; Liu et al., 2015). Huang et al. (Xiong et al., 2018) prepared a kind of two-dimensional Mo/Mo_2C heteronanosheets (Mo/Mo_2C-HNS) as an efficient and stable noble metal-free electrocatalyst toward the HER in 0.5 M H_2SO_4. Gao et al. (Lin et al., 2016) developed cobalt-doping into Mo_2C nanowires to effectively optimize the electron features around Fermi level, accomplishing the efficient HER

---

[1] Collaborative Innovation Center of Technology and Equipment for Biological Diagnosis and Therapy in Universities of Shandong, Institute for Advanced Interdisciplinary Research (iAIR), University of Jinan, Jinan 250022, P. R. China

[2] Guangzhou Key Laboratory for Surface Chemistry of Energy Materials, School of Environment and Energy, South China University of Technology, Guangzhou Higher Education Mega Center, Guangzhou 510006, P. R. China

[3] State Key Laboratory of Pulp and Paper Engineering, South China University of Technology, Guangzhou 510641, P. R. China

[4] State Key Laboratory of Crystal Materials, Shandong University, Jinan 250100, P. R. China

[5] These authors contributed equally

[6] Lead Contact

*Correspondence: hongliu@sdu.edu.cn (H.L.), ifc_zhouwj@ujn.edu.cn (W.Z.)

https://doi.org/10.1016/j.isci.2019.08.055

in both acidic and basic electrolytes. Therefore, to further improve HER activity of Mo_2C, the structure-activity relationship relying on controlled morphology and doping for enhancing exposure of surface active sites is demanded to be uncovered for rational catalyst design.

In addition, the agglomeration of catalysts, especially in the form of powder, can also lead to the loss of active sites (Chen et al., 2013). However, most of the as-synthesized nanoelectrocatalysts are in powder form, which need to be loaded onto glassy carbon (GC) electrodes with conductive polymer binders, such as Nafion. Unsatisfactorily, this step and the use of polymer materials will cause electrocatalysts agglomeration, which often leads to not only lower catalytic activity but also instability in the catalytic process (Asefa and Huang, 2017). Moreover, as long-term testing can cause Nafion to fall off from catalyst and electrode, resulting in poor contact between the catalyst particles and the underlying GC electrodes, the electron transfer from the electrode to electrocatalysts becomes difficult. Undoubtedly, Nafion is expensive and must undergo hazardous manufacturing processes, which is not suitable for large-scale practical applications (Liang et al., 2013; Dong et al., 2012; Kim et al., 2010). Therefore, it is urgently necessary to exploit a low-cost and readily available material that can bond the catalyst powder without reducing catalytic activity to replace the inconvenient artificial polymer, especially Nafion. Nanocelluloses (NCs), being an abundant and natural polymer with considerable physical and biological properties, including renewable resource, sustainability, excellent mechanical properties, biodegradability, and biocompatibility (Lin and Dufresne, 2014; Geyer et al., 1994), have been widely used in numerous fields such as electronics (Yan et al., 2014), medicine (Liu et al., 2007), tissue engineering (Zhang et al., 2015), and pharmacy (Zoppe et al., 2014). Moreover, nanocellulose possesses a superior hydrophilicity owing to the rich surface hydroxyl group, as well as high specific surface area and thermal stability, making it an advantageous carrier and binder for nanomaterials, especially in the powder form (Mo et al., 2009; Kaushik and Moores, 2016; Nyström et al., 2009).

In this work, we report nitrogen-doped molybdenum carbide nanobelts (N-Mo_2C NBs) with porous structure synthesized through a direct pyrolysis process using the pre-prepared molybdenum oxide nanobelts (MoO_3 NBs). Subsequently, nanocellulose instead of Nafion was employed in the bonding and fixing of N-Mo_2C NBs. Surprisingly, nanocellulose bonded N-Mo_2C NBs (N-Mo_2C@NCs) exhibited superior performance for HER, which possessed a lower overpotential (achieved 10 mA cm^{-2}) of 163 mV than Nafion bonded N-Mo_2C NBs (N-Mo_2C@Nafion) (180 mV) in an acidic electrolyte. To develop a simple and inexpensive methodology for practical applications, the flexible film electrode composed of N-Mo_2C NBs, graphene nanosheets, and nanocelluloses (N-Mo_2C/G@NCs) was fabricated by vacuum filtration. The obtained N-Mo_2C/G@NCs possessed a small onset potential of −41 mV versus RHE to reach 1 mA cm^{-2}, low Tafel slope (58.83 mA dec^{-1}), and superior long-term stability (remaining the current densities of 100 mA cm^{-2} for 100 h, 200 mA cm^{-2} for 77 h, and 300 mA cm^{-2} for 60 h with negligible degradation of 0.92%, 3.69%, and 4.04%, respectively) toward HER. This work not only proposed the potential of nanocellulose to replace Nafion for binding powder catalysts, but also offered a facile strategy to prepare flexible conductive film electrode for a wide variety of nanomaterials.

RESULTS AND DISCUSSION

Herein, we performed a detailed characterization of MoO_3 NBs and N-Mo_2C NBs. The MoO_3 NBs with smooth surface were successfully synthesized by hydrothermal reaction, which was confirmed by scanning electron microscopy (SEM) image (Figure 1A), transmission electron microscopy (TEM) images (Figure S1), and X-ray powder diffraction (XRD, Figure S2). After calcining MoO_3 NBs with dicyandiamide at 800°C for 2 h under Ar gas atmosphere, the prepared porous N-Mo_2C NBs were confirmed by the XRD pattern (Figure 1H, JCPDS No. 72–1683), in which the characteristic peaks at 34.47° (021), 38.07° (200), 39.53° (121), 52.29° (221), 61.76° (040), 69.77° (321), 74.90° (240), and 75.85° (142) were detected (Wang et al., 2017). Moreover, the SEM (Figures 1B and 1C) and TEM (Figures 1D and 1E) images indicated the nanobelt morphology of N-Mo_2C with the width of ~500 nm and length of 2–8 μm inherited from the pristine MoO_3 NBs. However, the rough and porous surface of N-Mo_2C NBs was observed. High-resolution transmission electron microscopy (HRTEM) image in Figure 1F revealed well-resolved lattice fringes with the interval distance of 0.223 nm that could be indexed to the (121) plane of Mo_2C phase. The element mapping result exhibited a homogeneous distribution of the N, C, and Mo elements in the resultant N-Mo_2C NBs (Figure 1G). Furthermore, the Brunauer-Emmett-Teller specific surface area of the porous N-Mo_2C NBs was determined by N_2 adsorption-desorption isotherm as 21.60 m^2 g^{-1}, which was larger than that of MoO_3 NBs (11.03 m^2 g^{-1}), causing the penetration of electrolyte to be promoted and rich active sites to

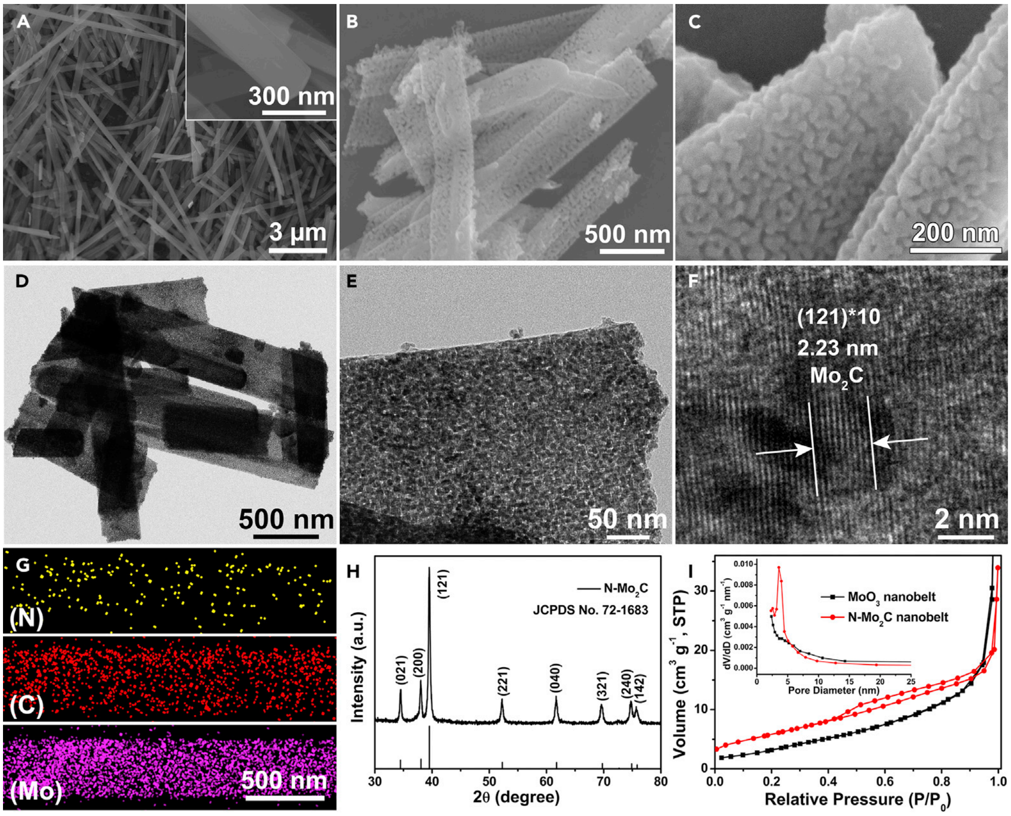

Figure 1. Morphology and Structural Characterization of MoO_3 NBs and N-Mo_2C NBs

(A–C) SEM images of (A) MoO_3 NBs and (B and C) N-Mo_2C NBs.

(D–H) (D and E) TEM images, (F) HRTEM image, (G) the elemental mapping, and (H) XRD pattern of N-Mo_2C NBs.

(I) The nitrogen adsorption-desorption isotherms and pore size distributions of MoO_3 NBs and N-Mo_2C NBs.

See also Figures S1–S3.

be exposed (Figure 1I) (Gao et al., 2016). Simultaneously, what we could get was that the pore size distribution of N-Mo_2C was below 10 nm (inset of Figure 1I). Subsequently, the thicknesses of MoO_3 NBs and N-Mo_2C NBs were measured by atomic force microscope, as demonstrated in Figure S3. It could be observed that the thickness of the N-Mo_2C NBs (~120 nm) was greater than that of MoO_3 NBs (~58 nm), which should be derived from the rough porous structure formed on the surface of the N-Mo_2C NBs, resulting in that N-Mo_2C NBs possessed a larger specific surface area and exposed more catalytically active sites.

Pleasantly, the N-Mo_2C was steadily dispersed in nanocellulose aqueous solution, which maintained 24 h with negligible precipitation, as shown in Figure 2A. However, the N-Mo_2C dispersed in both Nafion solution (Figure 2A) and aqueous solution (Figure S4) did not show satisfactory results. SEM was implemented to examine the morphologies and structures of N-Mo_2C@Nafion and N-Mo_2C@NCs in Figures S5 and S6. As displayed in Figure S5, through the Nafion link, the N-Mo_2C NBs were concentrated and buried, indicating that the use of Nafion would cause catalysts to aggregate and tightly cover catalysts, so that their active sites could not be fully exposed. On the contrary, in Figure S6, the morphology of the N-Mo_2C NBs was maintained, and the addition of nanocelluloses caused the nanobelts to be bonded together and well fixed. Simultaneously, the N-Mo_2C NBs could be fully released, which was beneficial to the exposure of active sites. To further confirm this point of view, the commercial 20 wt% Pt/C was taken the same dispersion in Nafion and nanocellulose solution. SEM in Figures S7 and S8 indicated that 20 wt% Pt/C@NCs possessed a higher exposure rate than that of 20 wt% Pt/C@Nafion.

Next, we investigated the HER electrocatalytic activity of N-Mo_2C@NCs modified GC electrode in an acidic electrolyte (0.5 M H_2SO_4), where the potential of the reference electrode was calibrated with

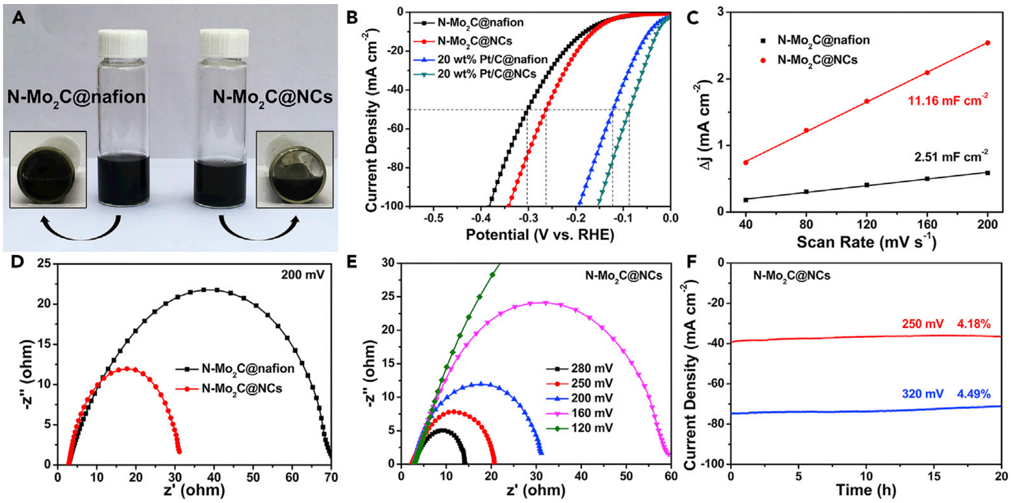

Figure 2. Comparison of Properties of Nafion- and Nanocellulose-Bonded Powder Catalysts

(A) Photos of N-Mo_2C aqueous dispersion with nanocelluloses and Nafion solutions, respectively.

(B) The LSV curves (without *iR* corrected) of N-Mo_2C@Nafion, N-Mo_2C@NCs, 20 wt% Pt/C@Nafion, and 20 wt% Pt/C@NCs.

(C and D) (C) Plot of positive and negative current density differences at a given potential (0.15 V versus the RHE) against the CV scan rates, and (D) EIS Nyquist plots at −200 mV versus RHE recorded of porous N-Mo_2C@Nafion and N-Mo_2C@NCs.

(E and F) (E) EIS Nyquist plots with different overpotentials and (F) the chronoamperometry curves recorded at the overpotentials of 250 and 320 mV driven from N-Mo_2C@NCs. All electrochemical tests were performed in 0.5 M H_2SO_4 solution.

See also Figures S4–S16.

respect to a reversible hydrogen electrode (RHE) performed in a high-purity H_2 (99.999%)-saturated electrolyte (Figure S9). For comparison, the electrocatalytic actives of N-Mo_2C@Nafion, 20 wt% Pt/C@Nafion, and 20 wt% Pt/C@NCs were also investigated as benchmarks under the same conditions, as displayed in Figure 2B. As expected, 20 wt% Pt/C@NCs behaved the best performance for HER among our catalysts, which only required an overpotential of 28 mV to reach a current density of 10 mA cm^{-2}, which was lower than that of 20 wt% Pt/C@Nafion catalyst (44 mV). Moreover, N-Mo_2C@NCs possessed an overpotential (achieved 10 mA cm^{-2}) of 163 mV lower than that of N-Mo_2C@Nafion catalyst (180 mV). When at a current density of 50 mA cm^{-2} or even higher, both 20 wt% Pt/C@NCs and N-Mo_2C@NCs exhibited significant potential reductions of ~38 mV compared with 20 wt% Pt/C@Nafion and N-Mo_2C@Nafion, respectively, indicating the potential of nanocellulose to replace Nafion for bonding powder catalysts. In addition, Tafel plots derived from Figure 2B indicated that the nanocellulose-bonded powder catalyst possessed a faster HER kinetics (Figure S10), further revealing the potential of nanocellulose to replace Nafion. The double-layer capacitance of N-Mo_2C@NCs and N-Mo_2C@Nafion was measured by cyclic voltammograms (CVs), which was a pivotal parameter for estimating the electrochemical area at the solid-liquid interface. The double-layer capacitance of N-Mo_2C@CNC (11.16 mF cm^{-2}) was extremely larger than that of N-Mo_2C@Nafion (2.51 mF cm^{-2}), as exhibited in Figures 2C and S11. The larger electrochemical area was associated with more active sites on the surface of N-Mo_2C@NCs at the solid-liquid interface, which was driven from the double-layer capacitance. The HER kinetics of N-Mo_2C@NCs and N-Mo_2C@Nafion at the electrode/electrolyte interface were further investigated in detail. In Figure 2D, the charge-transfer resistance (R_{ct}) of N-Mo_2C@NCs (31.8 Ω) was much lower than that of N-Mo_2C@Nafion (71.2 Ω), suggesting the favorable kinetics of N-Mo_2C@NCs during the HER process. Figure 2E showed the representative Nyquist plots of N-Mo_2C@NCs at various overpotentials. It could be seen that, as the overpotential increased, the diameter of the semicircle in the low frequency region decreased accordingly (60 Ω at 160 mV to 15 Ω at 280 mV), indicating a diminishment of R_{ct}. In addition, to study the durability of N-Mo_2C@NCs, long-term stability tests at the constant potentials (250 and 320 mV) have been operated. As shown in Figure 2F, N-Mo_2C@NCs displayed the current densities of 38 and 75 mA cm^{-2}, which remained stable for 20 h with minimal degradation. Compared with N-Mo_2C@NCs, it could be observed from Figure S12 that N-Mo_2C@Nafion exhibited the obvious attenuation of 15.8% after i-t testing for 20 h. Therefore, the nanocellulose that replaced Nafion as binding agent was found to enhance not only the HER activity, but also the stability of the electrocatalyst. To reflect the practicality of film formation, loading on the surface of the substrate (carbon fiber cloth, abbreviated as CFC) was also achieved, which effectively reduced the amount of catalyst slurry. As manifested in Figures S13 and S14, N-Mo_2C@NCs and 20 wt% Pt/C@NCs hybrid components were evenly distributed on the surface of carbon nanofibers.

In addition, to highlight the performance advantages of nanocellulose in bonding powder catalysts compared with Nafion as a binder, additional five powder catalysts were further obtained, which were cobalt nanoparticles encapsulated in nitrogen-doped carbon nanotubes (Co@N-C) obtained via an uncomplicated pyrolysis of Co-MOF (ZIF-67) (Yu et al., 2018a, 2018b), nitrogen-doped carbon nanotube-coated cobalt nanoparticles (Co@NC) by pyrolysis of cobalt salt with dicyandiamide, nitrogen-doped carbon nanotube-coated nickel nanoparticles (Ni@NC) by pyrolysis of nickel salt with dicyandiamide (Zou et al., 2014; Zhou et al., 2016a, 2016b), the Co_2P nanoparticles embedded into N, P co-doped carbon shells (Co_2P@NPC) derived from cobalt ions-adsorbed saccharomycete cells (Li et al., 2018), $MoSe_2$ nanosheet/MoO_2 nanobelt/carbon nanotube ($MoSe_2$/MoO_2/CNTs) composed of highly conductive CNTs, and hierarchical $MoSe_2$ nanosheets on MoO_2 nanobelts (Yang et al., 2018), respectively. The phase composition of the as-prepared Co@N-C, Co@NC, Ni@NC, Co_2P@NPC, and $MoSe_2$/MoO_2/CNTs catalysts could be confirmed by XRD results in Figure S15, which illustrated the successful preparation of the target samples. It could be seen from Figure S16 that the nanocellulose-linked catalysts exhibited better HER performance than the corresponding catalysts bonded by Nafion, further embodying the advantages of nanocellulose as a binder.

Conversely, flexible nanocellulose-based N-Mo_2C electrically conductive films were obtained by simple suction filtration on the resulted aqueous mixtures with nanocellulose linkages, as shown in Figure 3A. It is well known that the pure nanocellulose film exhibited network structure owing to the strong hydrogen bonding among the whiskers (Figure S17) (Nekouei et al., 2018; Liu et al., 2014). The nanocellulose could bind graphene nanosheets and N-Mo_2C nanobelts with hydrogen bonds of hydroxys, contributing to outstanding flexibility, which indicated that nanocellulose possessed the excellent bonding between cellulose nanowhiskers and N-Mo_2C nanobelts. Adding a small amount of graphene nanosheets was favored to enhance the conductivity. Particularly, nanocellulose played the key role in forming a flexible film. As shown on the right side of Figure 3B, a photo of an integrated N-Mo_2C film was presented, which possessed high flexibility so that it could be bent by 180° without breaking. Without nanocellulose, the N-Mo_2C/G could not form a film and was easy to powder, as shown in the left photo of Figure 3B. A physical film of N-Mo_2C@NCs was also demonstrated in Figure S18, formed by suction filtration only using N-Mo_2C nanobelts and nanocellulose, from which it could be observed that the effect of flexible film formation is due to the film-forming properties of nanocellulose, whereas enhanced conductive graphene nanosheets did not contribute to a film-forming effect. In addition, the obtained N-Mo_2C/G@NCs films could be easily tailored to pieces with appropriate size for practical applications. As shown in Figure 3C, hexagons, rectangles, triangles, and ribbon electrodes were rendered through the obtained films being cut, indicating that the film electrodes possessed unparalleled simplicity and convenience for the actual operation process.

To disclose a better performance of the N-Mo_2C/G@NCs than N-Mo_2C/G, the wettability was checked by measuring the contact angles toward sample surfaces. It could be seen from Figure 3D that the contact angles with water for N-Mo_2C/G and N-Mo_2C/G@NCs were measured as 74.20° and 23.40°, respectively, which meant that N-Mo_2C/G@NCs could display a more hydrophilic behavior than N-Mo_2C/G. Figure 3E manifested the Fourier transform infrared (FTIR) spectra of N-Mo_2C/G and N-Mo_2C/G@NCs. Compared with N-Mo_2C/G, the evident enhancement in the intensity of H-O bond at around 3,313 cm^{-1} indicated the formation of more hydroxyl groups on the N-Mo_2C/G@NCs surfaces caused by the addition of nanocellulose (Du et al., 2019; Hsu et al., 2019). In addition, N-Mo_2C/G@NCs showed peaks from 2,915 to 2,848 cm^{-1}, corresponding to the stretching vibrations of C-H (Du et al., 2019; Hsu et al., 2019), which demonstrated that N-Mo_2C/G has been successfully connected by nanocellulose in N-Mo_2C/G@NCs. X-ray photoelectron (XPS) spectra for O 1s of both samples could be deconvoluted to Mo-O or C-O (532.6 eV), and C=O (530.8 eV) bonds, except that there was a C-OH (531.4 eV) bond in N-Mo_2C/G@NCs (Lee et al., 2018), as shown in Figure 3F. Among them, Mo-O bond attributed to the surface oxidation of N-Mo2C NBs exposed to air (Huang et al., 2016), and C-OH bond owed to the introduction of

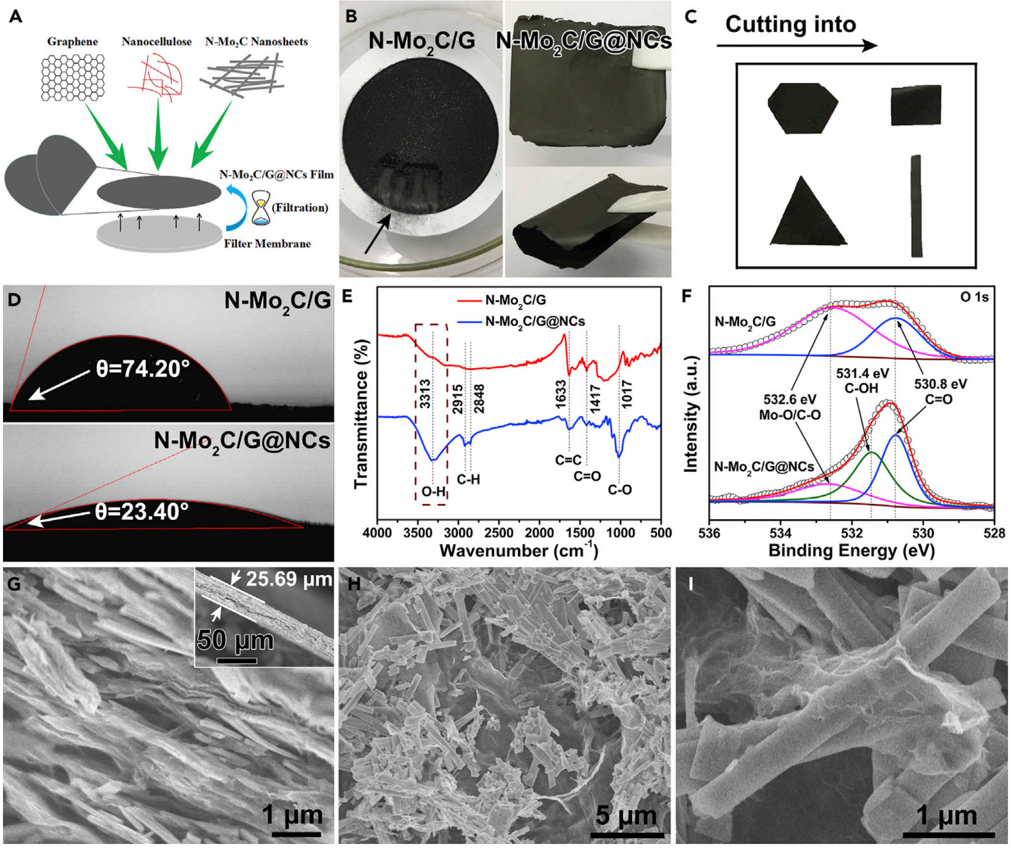

Figure 3. Characterization of Structural Properties of N-Mo$_2$C/G@NCs Film

(A) Schematic diagram of forming N-Mo$_2$C/G@NCs film.

(B) Photos of the nanocellulose-free N-Mo$_2$C/G filter membrane with a scraping operation (left) and free-standing flexible N-Mo$_2$C film (right).

(C) Physical images with N-Mo$_2$C/G@NCs electrodes cut into different shapes.

(D–I) (D) Contact angle measurement, (E) FTIR spectra, and (F) High-resolution XPS spectra for O 1s of N-Mo$_2$C/G and N-Mo$_2$C/G@NCs. SEM images with (G) cross-sectional view and (H and I) plane view of N-Mo$_2$C/G@NCs.

See also Figures S17–S24.

hydroxyl groups by adding nanocellulose (Figure S19), as well as that C-O and C=O bonds arised from partial oxidation of carbon in N-Mo2C/G@NCs and functional groups in nanocellulose.

Subsequently, the structure of N-Mo$_2$C/G@NCs was strictly characterized. It could be presented from the inset of Figure 3G that the N-Mo$_2$C/G@NCs film possessed a thickness of ~25.69 μm, which could be controlled by adding aqueous mixtures (Figure S20). And a wavy layered structure could be clearly observed from the cross section in Figure 3G, which possessed an open architecture for rapid diffusion of ion/electron, maximizing the exposure of the active sites of N-Mo$_2$C/G@NCs (Yang et al., 2018). As for the surface of N-Mo$_2$C/G@NCs film, the N-Mo$_2$C nanobelts and graphene nanosheets were observed and fully exposed, which provided a large number of catalytic active sites, as shown in Figures 3H and 3I. In contrast, the pure graphene nanosheets possessed a smooth surface (Figure S21), which limited the amount of supported electrocatalysts. At last, XRD (Figure S22), Raman (Figure S23), and XPS (Figure S24) results also confirmed the successful synthesis of N-Mo$_2$C/G@NCs.

The prepared N-Mo$_2$C/G@NCs could be directly used as 3D electrodes for HER. For comparison, N-Mo$_2$C@Nafion and N-Mo$_2$C/G@Nafion were loaded on CFC to construct 3D electrodes, which were investigated as electrocatalysts for HER. Conversely, bare CFC as supporter was nearly electrochemically inert for HER. The N-Mo$_2$C/G@NCs electrode exhibited excellent catalytic activity with an onset potential of −41 mV versus RHE, as displayed in Figure 4A. To drive a current density of 10 mA cm^{-2}, the

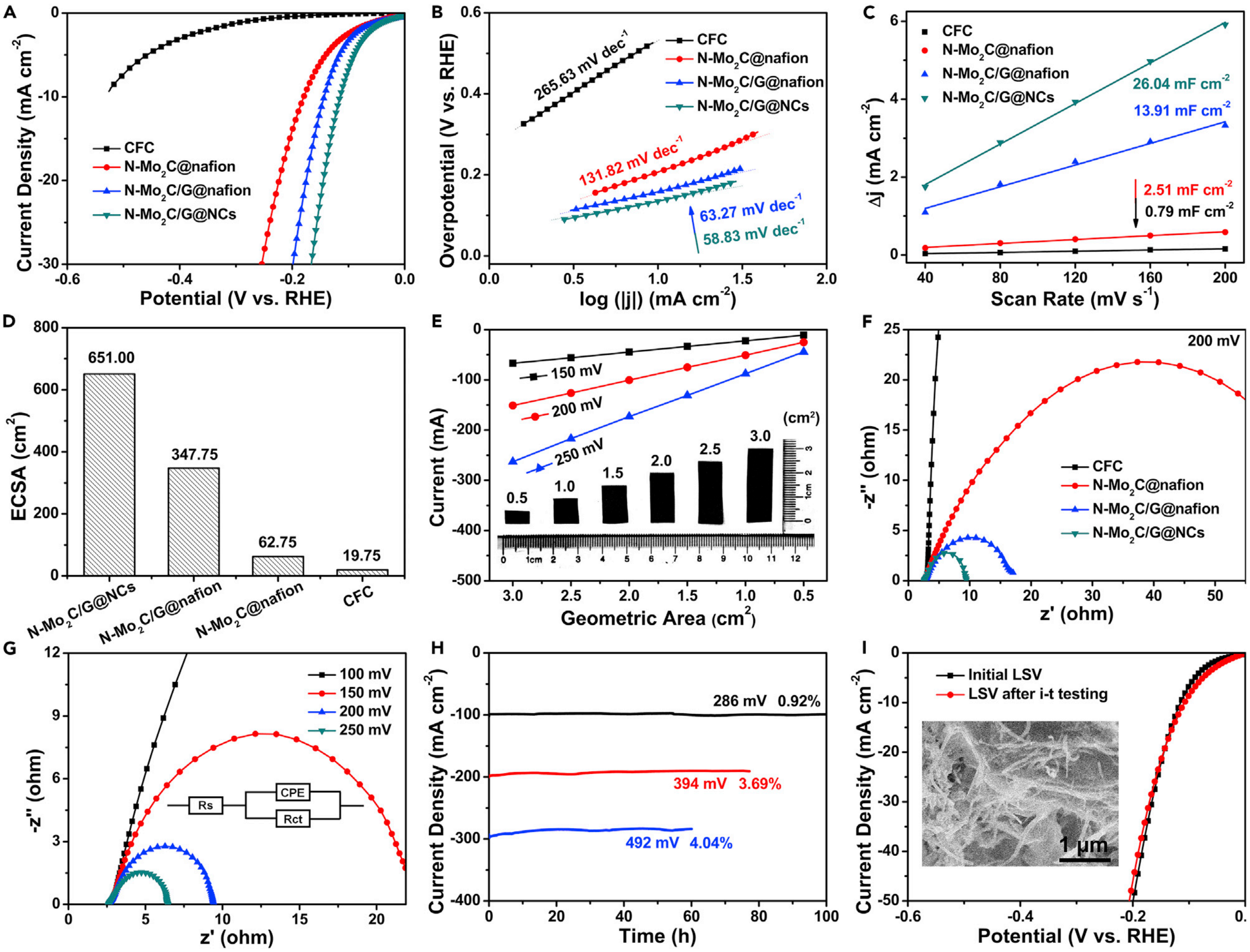

Figure 4. HER Performance of Bare CFC, N-Mo_2C@Nafion/CFC, N-Mo_2C/G@Nafion/CFC, and N-Mo_2C/G@NCs

(A and B) (A) The LSV curves (*iR* uncorrected) and (B) the corresponding Tafel plots of bare CFC, N-Mo_2C@Nafion/CFC, N-Mo_2C/G@Nafion/CFC, and N-Mo_2C/G@NCs.

(C and D) (C) Plot of positive and negative current density differences at a given potential (0.15 V versus RHE) against the CV scan rates, and (D) electrochemical active surface area (ECSA) of bare CFC, N-Mo_2C@Nafion/CFC, N-Mo_2C/G@Nafion/CFC, and N-Mo_2C/G@NCs electrodes.

(E) A plot of current for HER as a function of the geometric area from N-Mo_2C/G@NCs film under different overpotentials. The inset of (E) was the photos of N-Mo_2C/G@NCs with different geometric area.

(F) EIS Nyquist plots at −200 mV versus RHE recorded of bare CFC, N-Mo_2C@Nafion/CFC, N-Mo_2C/G@Nafion/CFC, and N-Mo_2C/G@NCs electrodes.

(G) EIS Nyquist plots of N-Mo_2C/G@NCs with different overpotentials.

(H) The chronoamperometry curves of the N-Mo_2C/G@NCs electrode recorded at the overpotentials of 286, 394, and 492 mV.

(I) The LSV curves of N-Mo_2C/G@NCs electrode after i-t testing. The inset of (I) displayed the corresponding SEM image after i-t testing. All tests were performed in 0.5 M H_2SO_4 solution.

See also Figures S25–S30.

N-Mo_2C/G@NCs electrode required an overpotential of 115 mV, which was much lower than those of N-Mo_2C@Nafion/CFC (178 mV) and N-Mo_2C/G@Nafion/CFC (143 mV). The above-mentioned comparison implied that the addition of nanocellulose instead of Nafion was beneficial to improve the HER performance of the N-Mo_2C catalyst. Furthermore, the HER kinetics of different samples were further evaluated by using the corresponding Tafel plots. As shown in Figure 4B, the Tafel slope of N-Mo_2C/G@NCs catalyst was calculated to be 58.83 mA dec^{-1}, which was much lower than those of bare CFC (265.63 mA dec^{-1}), N-Mo_2C@Nafion/CFC (131.82 mA dec^{-1}), and N-Mo_2C/G@Nafion/CFC (63.27 mA dec^{-1}), revealing the favorable HER kinetics over N-Mo_2C/G@NCs. According to three principal steps (Volmer, Heyrovsky, and Tafel steps) in the mechanism of hydrogen generation in acidic electrolytes (Huang et al., 2018; Jaramillo et al., 2007), the as-prepared N-Mo_2C/G@NCs electrocatalyst might proceed via a Volmer-Heyrovsky mechanism, where electrochemical desorption was the rate-limiting step (Xue et al., 2018; Cheng et al., 2017).

The electrochemical surface area (ECSA) of different samples was evaluated, using the electrical double-layer capacitance tested by CVs. From Figures 4C and S25, the double-layer capacitance value of N-Mo_2C/G@NCs was 26.04 mF cm^{-2}, which was 26.84, 10.37, and 1.87 times larger than those of bare CFC (0.97 mF cm^{-2}), N-Mo_2C@Nafion/CFC (2.51 mF cm^{-2}), and N-Mo_2C/G@Nafion/CFC (13.91 mF cm^{-2}), respectively. It was clearly found that the porous N-Mo_2C nanobelts added nanocellulose and graphene nanosheets could result in a high ECSA, which might be associated with the greatly enhanced electrocatalytic HER activity (Figure 4D) (Suen et al., 2017). To explore the exposure of the active sites of the catalysts when using hydroxy nanocellulose instead of Nafion, the turnover frequency (TOF) per active site was estimated (Zhang et al., 2019), which was calculated and plotted against potential in Figure S26. What could be observed was that the TOF value of N-Mo_2C/G@NCs (e.g., 0.37 s^{-1}@100 mV) was larger than that of N-Mo_2C/G@Nafion (e.g., 0.16 s^{-1}@100 mV) under the same potential, which well supported the result that nanocellulose used as a binder could be exposed more to catalytically active sites than Nafion. In addition, the geometric areas of electrode could also be easily manipulated owing to the editability of N-Mo_2C/G@NCs. It could be observed from Figure 4E that the current increased linearly with increasing geometric area of N-Mo_2C/G@NCs.

To explore the interfacial properties of obtained catalysts, electrochemical impedance spectroscopy (EIS) measurements at the overpotential of 200 mV were conducted. The Nyquist plots given in Figure 4F revealed that the charge-transfer resistance (R_{ct}) of N-Mo_2C/G@NCs (9.5 Ω) was obviously lower than those of bare CFC (>1500 Ω), N-Mo_2C@Nafion/CFC (72.9 Ω), and N-Mo_2C/G@Nafion/CFC (17.5 Ω), thus achieving the lowest charge-transfer resistance among all the as-synthesized electrocatalysts, which implied the fastest and most efficient charge transport of N-Mo_2C/G@NCs during the electrocatalytic HER process (Li et al., 2018). Furthermore, the typical Nyquist plots of N-Mo_2C/G@NCs electrode at various overpotentials are displayed in Figure 4G, where the fitting parameters of R_s and CPE were 2.57 and 0.84 Ω, respectively. It could be seen that the R_{ct} values of N-Mo_2C/G@NCs significantly decreased with increasing overpotentials, from 83.67 Ω at 100 mV to 6.44 Ω at 250 mV, which indicated the fast reaction rate and favorable HER kinetics at the electrode/electrolyte interface (Zhou et al., 2016a, 2016b).

In addition to catalytic activity, electrochemical stability was another crucial factor in evaluating the properties of synthetic materials. The long-term stability of N-Mo_2C/G@NCs electrode was performed by continuous electrolysis at three fixed overpotentials of 286, 394, and 492 mV in 0.5 M H_2SO_4. Obviously, the current densities of 100 mA cm^{-2} for 100 h, 200 mA cm^{-2} for 77 h, 300 mA cm^{-2} for 60 h were rather stable, possessing negligible degradation of 0.92%, 3.69%, and 4.04%, respectively, as demonstrated in the time-dependent current density curves of Figure 4H. Furthermore, no obvious changes were observed in the LSV curves after i-t testing investigated by the above-mentioned continuous electrolysis (Figure 4I), revealing the excellent electrocatalytic stability of the N-Mo_2C/G@NCs electrode for HER. At the same time, the corresponding electrode maintained a complete morphology in the inset of Figures 4I and S27, indicating its superior structural stability. By comparing XPS survey spectrum after prolonged i-t testing with the initial survey spectrum in Figure S28, the stability of the chemical elements of N-Mo_2C/G@NCs could be observed. Therefore, the excellent performance of the N-Mo_2C/G@NCs electrode could be attributed to the following. First, nitrogen doping could increase electrocatalytic activity of Mo_2C. Second, the porous nanobelt structure exposed the N-Mo_2C catalyst to more catalytically active sites. Third, graphite nanosheet enhanced conductivity of N-Mo_2C/G@NCs. Fourth, nanocellulose with more hydroxyl groups increased the hydrophilicity of the electrode. Fifth, film formation could avoid the shedding of Nafion and powder catalyst, making its performance and structure stable.

In addition, to highlight the universality of this supported film method, we selected the above-mentioned five powder catalysts for surface filming operations, which were further characterized and tested. After the film formation of the powder catalysts on the surface of CFC, the corresponding SEM images of the synthesized Co@N-C/G@NCs, Co@NC/G@NCs, Ni@NC/G@NCs, Co_2P@NPC/G@NCs, and $MoSe_2$/MoO_2/CNTs/G@NCs were presented in Figure S29. On the one hand, under the film forming using graphene and nanocellulose, the morphology of the powder catalysts was maintained. On the other hand, the catalysts were uniformly dispersed on the surface of the carbon fiber. Moreover, the detailed electrochemical data of these flexible electrodes were shown in Figure S30. Therefore, the above-mentioned results indicated that the obtained powder catalyst could be efficiently loaded and filmed to form a flexible material through cross-linking with the one-dimensional structure of nanocelluloses and two-dimensional structure of graphene nanosheets.

Conclusion

In conclusion, we have proposed the nanocellulose to replace Nafion for binding powder catalysts and offered a facile strategy to prepare flexible conductive film electrode with porous N-Mo_2C nanobelts, graphene nanosheets, and nanocellulose. When at a current density of 50 mA cm^{-2} or even higher, both 20 wt% Pt/C@NCs and N-Mo_2C@NCs exhibited significant potential reduction (approximately 38 mV) compared with 20 wt% Pt/C@Nafion and N-Mo_2C@Nafion, respectively, indicating the potential of nanocellulose to replace Nafion for bonding powder catalysts. In addition, the flexible editable N-Mo_2C/G@NCs film was fabricated by vacuum filtration, possessing a wavy layered structure, which exhibited a small onset potential of -41 mV versus RHE, low Tafel slope of 58.83 mA dec^{-1}, and superior long-term stability (remaining the current densities of 100 mA cm^{-2} for 100 h, 200 mA cm^{-2} for 77 h, 300 mA cm^{-2} for 60 h without negligible degradation of 0.92%, 3.69%, and 4.04%, respectively) toward HER in 0.5 M H_2SO_4. It was determined that the present methodology developed paved the way for practical applications of that the powder catalyst was bonded with nanocellulose to replace Nafion and further formed a flexible film for energy storage and conversion.

Limitations of the Study

This work proposes the potential that nanocellulose can replace Nafion for binding powder catalysts. Although the experimental conclusions are further illustrated by different catalysts, the different catalysts for nanocellulose bonding demonstrate different degrees of improvement of electrocatalytic activity for HER, which may be limited by the properties of the applied catalysts. In addition, it can be observed from the work that functional group modification of nanocellulose or other organic reagents can be performed in subsequent studies to obtain a highly efficient alternative to Nafion-like binders.

METHODS

All methods can be found in the accompanying Transparent Methods supplemental file.

SUPPLEMENTAL INFORMATION

Supplemental Information can be found online at https://doi.org/10.1016/j.isci.2019.08.055.

ACKNOWLEDGMENTS

This work was supported by Guangdong Natural Science Funds for Distinguished Young Scholar (2017B030306001), Taishan Scholars Project Special Funds, Natural Science Foundation of Shandong Province (ZR2019YQ20), and Guangdong Innovative and Entrepreneurial Research Team Program (2014ZT05N200).

AUTHOR CONTRIBUTIONS

G.L. analyzed the data and wrote the manuscript. G.L., J.Y., Z.Z., and Z.X. conducted the synthetic experiments. G.L., J.Y., and R.L. performed material characterization. G.L., Q.C., Z.Z., and L.Z. conducted electrochemical performance for hydrogen evolution reaction. J.Y., Z.Z., Q.C., R.L., and L.Z. executed the paper modification. X.W. and X.P. served as a guide for flexible film preparation. W.Z. and H.L., as supervisors, designed the project and provided guidance, as well as financial support.

DECLARATION OF INTERESTS

The authors declare no competing interests.

Received: June 7, 2019
Revised: July 29, 2019
Accepted: August 27, 2019
Published: September 27, 2019

REFERENCES

Asefa, T., and Huang, X. (2017). Heteroatom-doped carbon materials for electrocatalysis. Chem. Eur. J. *23*, 10703–10713.

Chen, W.F., Wang, C.H., Sasaki, K., Marinkovic, N., Xu, W., Muckerman, J.T., Zhu, Y., and Adzic, R.R. (2013). Highly active and durable nanostructured molybdenum carbide electrocatalysts for hydrogen production. Energy Environ. Sci. *6*, 943–951.

Cheng, Y., Lu, S., Liao, F., Liu, L., Li, Y., and Shao, M. (2017). Rh-MoS_2 nanocomposite catalysts with Pt-like activity for hydrogen evolution reaction. Adv. Funct. Mater. *27*, 1700359.

Deng, S., Yang, F., Zhang, Q., Zhong, Y., Zeng, Y., Lin, S., Wang, X., Lu, X., Wang, C.-Z., Gu, L., et al. (2018). Phase modulation of (1T-2H)-$MoSe_2$/TiC-C shell/core arrays via nitrogen doping for highly efficient hydrogen evolution reaction. Adv. Mater. *30*, 1802223.

Dong, H., Yu, H., Wang, X., Zhou, Q., and Feng, J. (2012). A novel structure of scalable air-cathode without Nafion and Pt by rolling activated carbon and PTFE as catalyst layer in microbial fuel cells. Water Res. *46*, 5777–5787.

Dresselhaus, M.S., and Thomas, I.L. (2001). Alternative energy technologies. Nature *414*, 332.

Du, X., Du, W., Wang, Z., Liu, K., and Li, S. (2019). Defects in graphene nanoplatelets and their interface behavior to reinforce magnesium alloys. Appl. Surf. Sci. *484*, 414–423.

Fang, Y., Xue, Y., Hui, L., Yu, H., Liu, Y., Xing, C., Lu, F., He, F., Liu, H., and Li, Y. (2019). In situ growth of graphdiyne based heterostructure: toward efficient overall water splitting. Nano Energy *59*, 591–597.

Gao, X., Zhang, H., Li, Q., Yu, X., Hong, Z., Zhang, X., Liang, C., and Lin, Z. (2016). Hierarchical $NiCo_2O_4$ hollow microcuboids as bifunctional electrocatalysts for overall water-splitting. Angew. Chem. Int. Ed. *128*, 6398–6402.

Geng, X., Sun, W., Wu, W., Chen, B., Al-Hilo, A., Benamara, M., Zhu, H., Watanabe, F., Cui, J., and Chen, T.-P. (2016). Pure and stable metallic phase molybdenum disulfide nanosheets for hydrogen evolution reaction. Nat. Commun. *7*, 10672.

Geyer, U., Heinze, T., Stein, A., Klemm, D., Marsch, S., Schumann, D., and Schmauder, H.P. (1994). Formation, derivatization and applications of bacterial cellulose. Int. J. Biol. Macromol. *16*, 343–347.

Gray, H.B. (2009). Powering the planet with solar fuel. Nat. Chem. *1*, 7.

Hsu, H.H., Khosrozadeh, A., Li, B., Luo, G., Xing, M., and Zhong, W. (2019). An eco-friendly, nanocellulose/RGO/in situ formed polyaniline for flexible and free-standing supercapacitors. ACS Sustain. Chem. Eng. *7*, 4766–4776.

Huang, Y., Gong, Q., Song, X., Feng, K., Nie, K., Zhao, F., Wang, Y., Zeng, M., Zhong, J., and Li, Y. (2016). Mo_2C nanoparticles dispersed on hierarchical carbon microflowers for efficient electrocatalytic hydrogen evolution. ACS Nano *10*, 11337–11343.

Huang, Y., Ge, J., Hu, J., Zhang, J., Hao, J., and Wei, Y. (2018). Nitrogen-doped porous molybdenum carbide and phosphide hybrids on a carbon matrix as highly effective electrocatalysts for the hydrogen evolution reaction. Adv. Energy Mater. *8*, 1701601.

Hui, L., Xue, Y., Yu, H., Liu, Y., Fang, Y., Xing, C., Huang, B., and Li, Y. (2019). Highly efficient and selective generation of ammonia and hydrogen on a graphdiyne-based catalyst. J. Am. Chem. Soc. https://doi.org/10.1021/jacs.9b03004.

Humagain, G., MacDougal, K., MacInnis, J., Lowe, J.M., Coridan, R.H., MacQuarrie, S., and Dasog, M. (2018). Highly efficient, biochar-derived molybdenum carbide hydrogen evolution electrocatalyst. Adv. Energy Mater. *8*, 1801461.

Jaramillo, T.F., Jørgensen, K.P., Bonde, J., Nielsen, J.H., Horch, S., and Chorkendorff, I. (2007). Identification of active edge sites for electrochemical H_2 evolution from MoS_2 nanocatalysts. Science *317*, 100.

Kaushik, M., and Moores, A. (2016). Review: nanocelluloses as versatile supports for metal nanoparticles and their applications in catalysis. Green. Chem. *18*, 622–637.

Kim, S., Yan, J., Schwenzer, B., Zhang, J., Li, L., Liu, J., Yang, Z., and Hickner, M.A. (2010). Cycling performance and efficiency of sulfonated poly (sulfone) membranes in vanadium redox flow batteries. Electrochem. Commun. *12*, 1650–1653.

Koper, M.T.M. (2013). A basic solution. Nat. Chem. *5*, 255.

Lee, J., Oh, J., Jeon, Y., and Piao, Y. (2018). Multi-heteroatom-doped hollow carbon attached on graphene using $LiFePO_4$ nanoparticles as hard templates for high-performance lithium–sulfur batteries. ACS Appl. Mater. Interfaces *10*, 26485–26493.

Li, G., Yu, J., Jia, J., Yang, L., Zhao, L., Zhou, W., and Liu, H. (2018). Cobalt–cobalt phosphide Nanoparticles@Nitrogen-phosphorus doped carbon/graphene derived from cobalt ions adsorbed saccharomycete yeasts as an efficient, stable, and large-current-density electrode for hydrogen evolution reactions. Adv. Funct. Mater. *28*, 1801332.

Liang, X., Zhang, F., Feng, W., Zou, X., Zhao, C., Na, H., Liu, C., Sun, F., and Zhu, G. (2013). From metal–organic framework (MOF) to MOF–polymer composite membrane: enhancement of low-humidity proton conductivity. Chem. Sci. *4*, 983–992.

Lin, N., and Dufresne, A. (2014). Nanocellulose in biomedicine: current status and future prospect. Eur. Polym. J. *59*, 302–325.

Lin, H., Liu, N., Shi, Z., Guo, Y., Tang, Y., and Gao, Q. (2016). Cobalt-doping in molybdenum-carbide nanowires toward efficient electrocatalytic hydrogen evolution. Adv. Funct. Mater. *26*, 5590–5598.

Liu, Z., Sharma, B.K., and Erhan, S.Z. (2007). From oligomers to molecular giants of soybean oil in supercritical carbon dioxide medium: 1. Preparation of polymers with lower molecular weight from soybean oil. Biomacromolecules *8*, 233–239.

Liu, D.Y., Sui, G.X., and Bhattacharyya, D. (2014). Synthesis and characterisation of nanocellulose-based polyaniline conducting films. Compos. Sci. Technol. *99*, 31–36.

Liu, Y., Yu, G., Li, G.-D., Sun, Y., Asefa, T., Chen, W., and Zou, X. (2015). Coupling Mo_2C with nitrogen-rich nanocarbon leads to efficient hydrogen-evolution electrocatalytic sites. Angew. Chem. Int. Ed. *127*, 10902–10907.

Mo, Z.-l., Zhao, Z.-l., Chen, H., Niu, G.-p., and Shi, H.-f. (2009). Heterogeneous preparation of cellulose–polyaniline conductive composites with cellulose activated by acids and its electrical properties. Carbohydr. Polym. *75*, 660–664.

Nekouei, F., Nekouei, S., and Kargarzadeh, H. (2018). Enhanced adsorption and catalytic oxidation of ciprofloxacin on hierarchical CuS hollow nanospheres@N-doped cellulose nanocrystals hybrid composites: kinetic and radical generation mechanism studies. Chem. Eng. J. *335*, 567–578.

Nyström, G., Razaq, A., Strømme, M., Nyholm, L., and Mihranyan, A. (2009). Ultrafast all-polymer paper-based batteries. Nano Lett. *9*, 3635–3639.

Shi, Y., and Zhang, B. (2016). Recent advances in transition metal phosphide nanomaterials: synthesis and applications in hydrogen evolution reaction. Chem. Soc. Rev. *45*, 1529–1541.

Suen, N.-T., Hung, S.-F., Quan, Q., Zhang, N., Xu, Y.-J., and Chen, H.M. (2017). Electrocatalysis for the oxygen evolution reaction: recent development and future perspectives. Chem. Soc. Rev. *46*, 337–365.

Turner, J.A. (2004). Sustainable hydrogen production. Science *305*, 972.

Voiry, D., Fullon, R., Yang, J., de Carvalho Castro e Silva, C., Kappera, R., Bozkurt, I., Kaplan, D., Lagos, M.J., Batson, P.E., Gupta, G., et al. (2016). The role of electronic coupling between substrate and 2D MoS_2 nanosheets in electrocatalytic production of hydrogen. Nat. Mater. *15*, 1003.

Vrubel, H., and Hu, X. (2012). Molybdenum boride and carbide catalyze hydrogen evolution in both acidic and basic solutions. Angew. Chem. Int. Ed. *124*, 12875–12878.

Walter, M.G., Warren, E.L., McKone, J.R., Boettcher, S.W., Mi, Q., Santori, E.A., and Lewis, N.S. (2010). Solar water splitting cells. Chem. Rev. *110*, 6446–6473.

Wan, C., Regmi, Y.N., and Leonard, B.M. (2014). Multiple phases of molybdenum carbide as electrocatalysts for the hydrogen evolution reaction. Angew. Chem. Int. Ed. *126*, 6525–6528.

Wang, S., Wang, J., Zhu, M., Bao, X., Xiao, B., Su, D., Li, H., and Wang, Y. (2015). Molybdenum-carbide-modified nitrogen-doped carbon vesicle encapsulating nickel nanoparticles: a highly efficient, low-cost catalyst for hydrogen evolution reaction. J. Am. Chem. Soc. *137*, 15753–15759.

Wang, J., Cui, W., Liu, Q., Xing, Z., Asiri, A.M., and Sun, X. (2016). Recent progress in cobalt-based heterogeneous catalysts for electrochemical water splitting. Adv. Mater. *28*, 215–230.

Wang, H., Sun, C., Cao, Y., Zhu, J., Chen, Y., Guo, J., Zhao, J., Sun, Y., and Zou, G. (2017). Molybdenum carbide nanoparticles embedded in nitrogen-doped porous carbon nanofibers as a dual catalyst for hydrogen evolution and oxygen reduction reactions. Carbon *114*, 628–634.

Wu, H.B., Xia, B.Y., Yu, L., Yu, X.-Y., and Lou, X.W. (2015). Porous molybdenum carbide nano-octahedrons synthesized via confined carburization in metal-organic frameworks for efficient hydrogen production. Nat. Commun. *6*, 6512.

Xiao, P., Sk, M.A., Thia, L., Ge, X., Lim, R.J., Wang, J.-Y., Lim, K.H., and Wang, X. (2014). Molybdenum phosphide as an efficient electrocatalyst for the hydrogen evolution reaction. Energy Environ. Sci. *7*, 2624–2629.

Xie, J., Zhang, J., Li, S., Grote, F., Zhang, X., Zhang, H., Wang, R., Lei, Y., Pan, B., and Xie, Y. (2014). Correction to controllable disorder engineering in oxygen-incorporated MoS_2 ultrathin nanosheets for efficient hydrogen evolution. J. Am. Chem. Soc. *136*, 1680.

Xing, Z., Liu, Q., Asiri, A.M., and Sun, X. (2014). Closely interconnected network of molybdenum phosphide nanoparticles: a highly efficient electrocatalyst for generating hydrogen from water. Adv. Mater. *26*, 5702–5707.

Xiong, J., Li, J., Shi, J., Zhang, X., Suen, N.-T., Liu, Z., Huang, Y., Xu, G., Cai, W., Lei, X., et al. (2018). In situ engineering of double-phase interface in Mo/Mo_2C heteronanosheets for boosted hydrogen evolution reaction. ACS Energy Lett. *3*, 341–348.

Xu, X., Nosheen, F., and Wang, X. (2016). Ni-decorated molybdenum carbide hollow structure derived from carbon-coated metal–organic framework for electrocatalytic hydrogen evolution reaction. Chem. Mater. *28*, 6313–6320.

Xue, Y., Huang, B., Yi, Y., Guo, Y., Zuo, Z., Li, Y., Jia, Z., Liu, H., and Li, Y. (2018). Anchoring zero valence single atoms of nickel and iron on graphdiyne for hydrogen evolution. Nat. Commun. *9*, 1460.

Yan, C., Wang, J., Kang, W., Cui, M., Wang, X., Foo, C.Y., Chee, K.J., and Lee, P.S. (2014). Highly stretchable piezoresistive graphene–nanocellulose nanopaper for strain sensors. Adv. Mater. *26*, 2022–2027.

Yang, X., Feng, X., Tan, H., Zang, H., Wang, X., Wang, Y., Wang, E., and Li, Y. (2016). N-Doped graphene-coated molybdenum carbide nanoparticles as highly efficient electrocatalysts for the hydrogen evolution reaction. J. Mater. Chem. A *4*, 3947–3954.

Yang, L.J., Deng, Y.Q., Zhang, X.F., Liu, H., and Zhou, W.J. (2018). $MoSe_2$ nanosheet/MoO_2 nanobelt/carbon nanotube membrane as flexible and multifunctional electrodes for full water splitting in acidic electrolyte. Nanoscale *10*, 9268–9275.

Yu, J., Li, G., Liu, H., Wang, A., Yang, L., Zhou, W., Hu, Y., and Chu, B. (2018a). Simultaneous water recovery and hydrogen production by bifunctional electrocatalyst of nitrogen-doped carbon nanotubes protected cobalt nanoparticles. Int. J. Hydrogen Energy *43*, 12110–12118.

Yu, H., Xue, Y., Hui, L., Zhang, C., Li, Y., Zuo, Z., Zhao, Y., Li, Z., and Li, Y. (2018b). Efficient hydrogen production on a 3D flexible heterojunction material. Adv. Mater. *30*, 1707082.

Yu, H., Xue, Y., Huang, B., Hui, L., Zhang, C., Fang, Y., Liu, Y., Zhao, Y., Li, Y., Liu, H., and Li, Y. (2019). Ultrathin nanosheet of graphdiyne-supported palladium atom catalyst for efficient hydrogen production. iScience *11*, 31–41.

Zeng, L., Yang, L., Lu, J., Jia, J., Yu, J., Deng, Y., Shao, M., and Zhou, W. (2018). One-step synthesis of Fe-Ni hydroxide nanosheets derived from bimetallic foam for efficient electrocatalytic oxygen evolution and overall water splitting. Chin. Chem. Lett. *29*, 1875–1878.

Zhang, Y., Sargent, J.L., Boudouris, B.W., and Phillip, W.A. (2015). Nanoporous membranes generated from self-assembled block polymer precursors: Quo Vadis? J. Appl. Polym. Sci. *132*, 21.

Zhang, Y., Ouyang, B., Xu, J., Chen, S., Rawat, R.S., and Fan, H.J. (2016). 3D porous hierarchical nickel–molybdenum nitrides synthesized by RF plasma as highly active and stable hydrogen-evolution-reaction electrocatalysts. Adv. Energy Mater. *6*, 1600221.

Zhang, L., Jia, Y., Liu, H., Zhuang, L., Yan, X., Lang, C., Wang, Xi., Yang, D., Huang, K., Feng, S., and Yao, X. (2019). Charge polarization from atomic metals on adjacent graphitic layers for enhancing the hydrogen evolution reaction. Angew. Chem. Int. Ed. *58*, 9404–9408.

Zhao, Y., Kamiya, K., Hashimoto, K., and Nakanishi, S. (2015). In situ CO_2-emission assisted synthesis of molybdenum carbonitride nanomaterial as hydrogen evolution electrocatalyst. J. Am. Chem. Soc. *137*, 110–113.

Zhou, W., Lu, J., Zhou, K., Yang, L., Ke, Y., Tang, Z., and Chen, S. (2016a). $CoSe_2$ nanoparticles embedded defective carbon nanotubes derived from MOFs as efficient electrocatalyst for hydrogen evolution reaction. Nano Energy *28*, 143–150.

Zhou, W., Xiong, T., Shi, C., Zhou, J., Zhou, K., Zhu, N., Li, L., Tang, Z., and Chen, S. (2016b). Bioreduction of precious metals by microorganism: efficient gold@N-doped carbon electrocatalysts for the hydrogen evolution reaction. Angew. Chem. Int. Ed. *55*, 8416–8420.

Zoppe, J.O., Ruottinen, V., Ruotsalainen, J., Rönkkö, S., Johansson, L.-S., Hinkkanen, A., Järvinen, K., and Seppälä, J. (2014). Synthesis of cellulose nanocrystals carrying tyrosine sulfate mimetic ligands and inhibition of alphavirus infection. Biomacromolecules *15*, 1534–1542.

Zou, X., Huang, X., Goswami, A., Silva, R., Sathe, B.R., Mikmeková, E., and Asefa, T. (2014). Cobalt-embedded nitrogen-rich carbon nanotubes efficiently catalyze hydrogen evolution reaction at all pH values. Angew. Chem. Int. Ed. *53*, 4372–4376.

ISCI, Volume *19*

Supplemental Information

N-Doped Mo_2C Nanobelts/Graphene Nanosheets Bonded with Hydroxy Nanocellulose as Flexible and Editable Electrode for Hydrogen Evolution Reaction

Guixiang Li, Jiayuan Yu, Ziqian Zhou, Renkun Li, Zhihua Xiang, Qing Cao, Lili Zhao, Xiwen Wang, Xinwen Peng, Hong Liu, and Weijia Zhou

Supplemental Information

Supplemental Figures

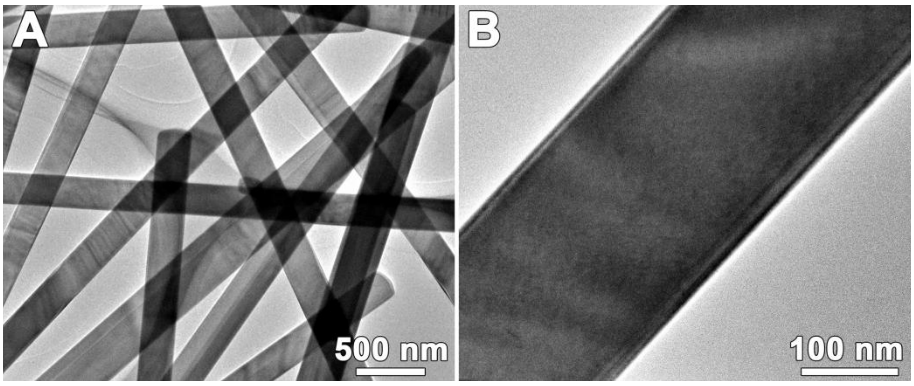

Figure S1. TEM images of MoO_3 nanobelts, related to **Figure 1**.

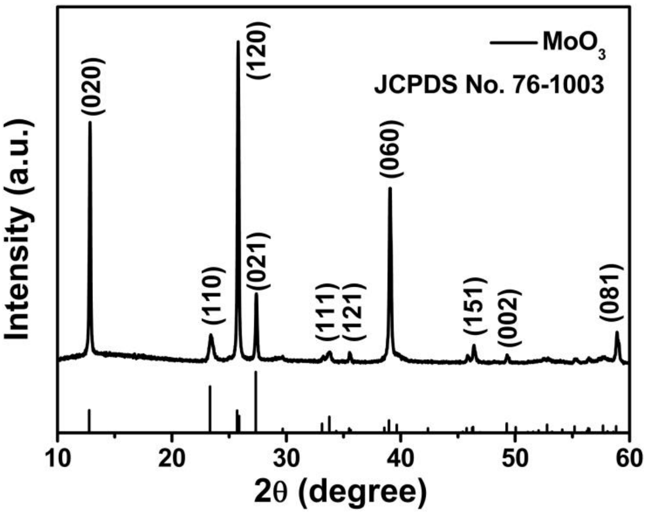

Figure S2. XRD pattern of MoO_3 nanobelt, related to **Figure 1**.

As displayed in **Figure S2**, the typical XRD peaks at around 12.77°, 23.33°, 25.88°, 27.32°, 33.76°, 35.62°, 38.97°, 46.92°, 49.26°, and 58.83° were corresponding to the (020), (110), (120), (021), (111), (121), (060), (151), (002), and (081) planes of MoO_3 (JCPDS No. 76-1003), respectively.

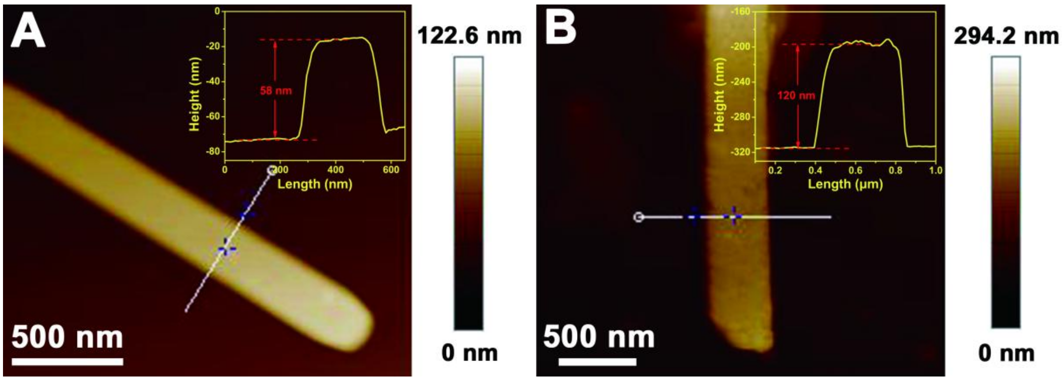

Figure S3. AFM measurement of typical (A) MoO_3 NBs and (B) N-Mo_2C NBs. Inset: Line scans of the height across the corresponding samples, related to **Figure 1**.

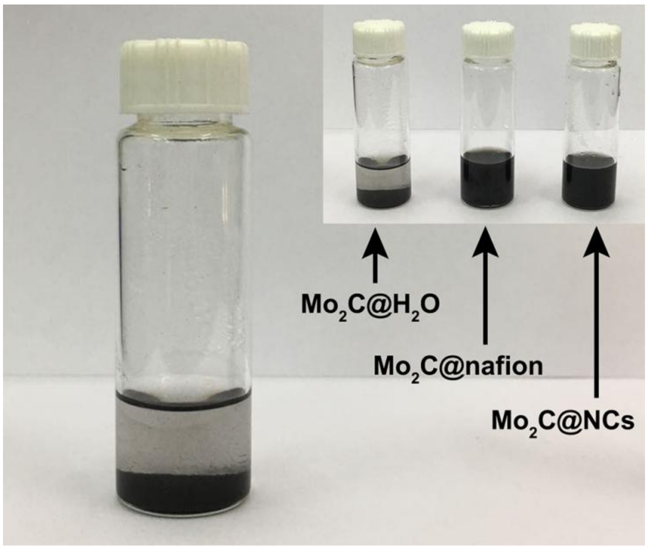

Figure S4. Photo of N-Mo_2C aqueous dispersion after standing for 24 h, related to **Figure 2**.

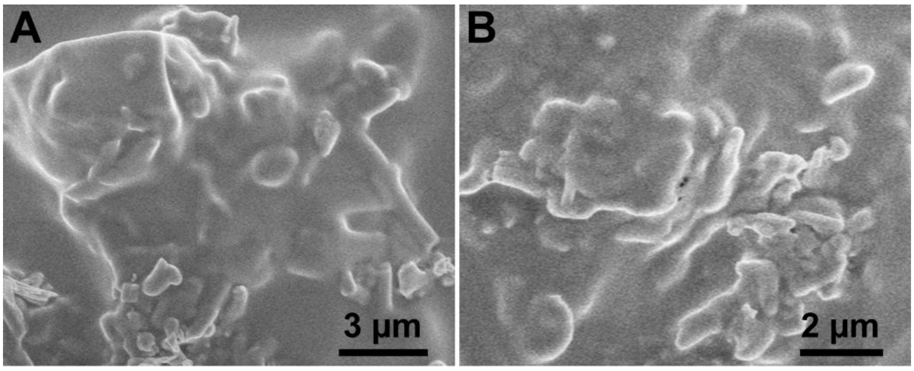

Figure S5. SEM images of N-Mo_2C@nafion aqueous dispersion dried on the GC electrode, related to **Figure 2**.

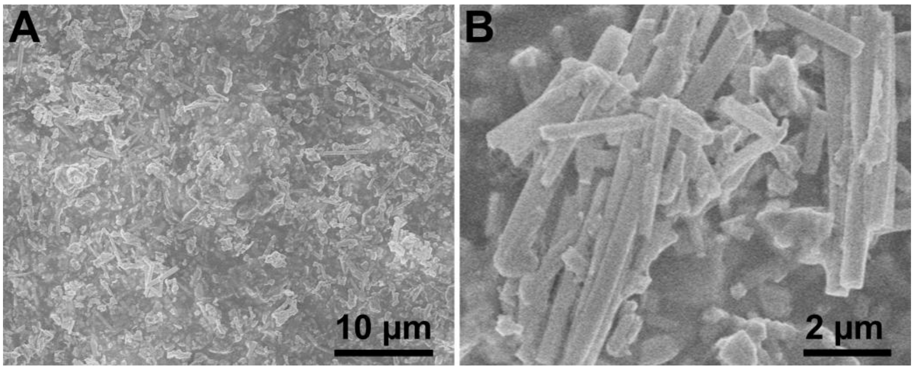

Figure S6. SEM images of N-Mo_2C@NCs aqueous dispersion dried on the GC electrode, related to **Figure 2**.

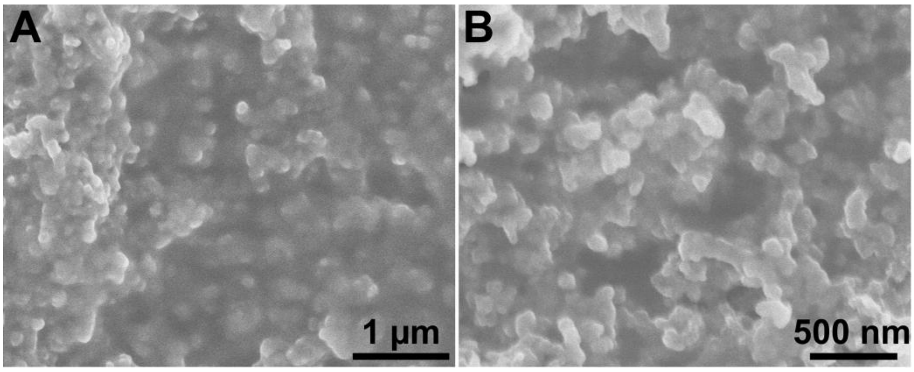

Figure S7. SEM images of 20 wt% Pt/C@nafion aqueous dispersion dried on the GC electrode, related to **Figure 2**.

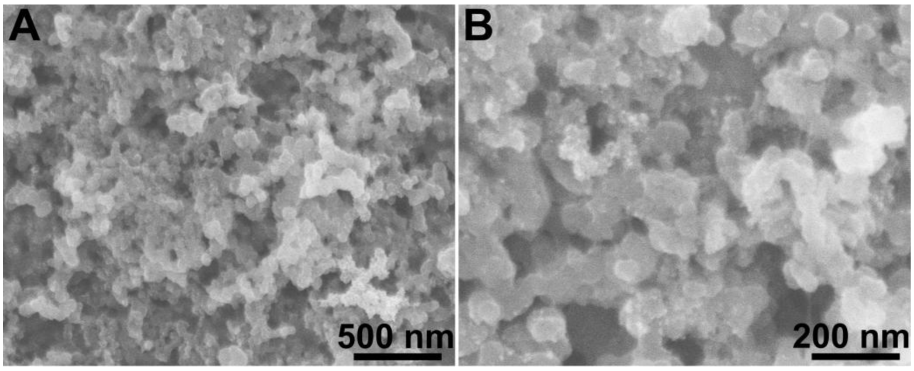

Figure S8. SEM images of 20 wt% Pt/C@NCs aqueous dispersion dried on the GC electrode, related to **Figure 2**.

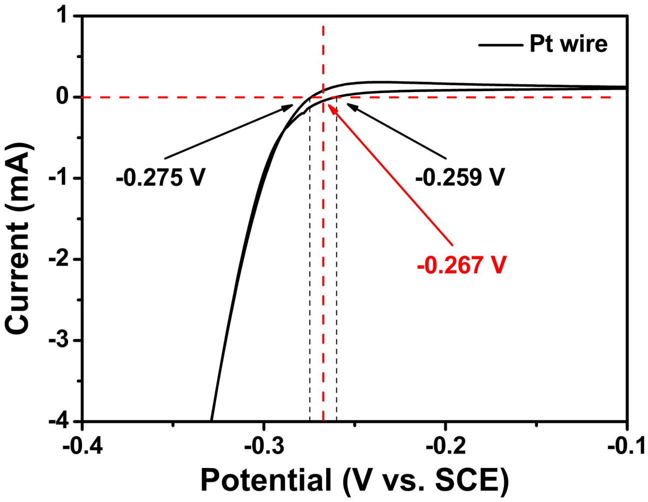

Figure S9. The calibration of reference electrode potential recorded by CV curve, related to **Figure 2**.

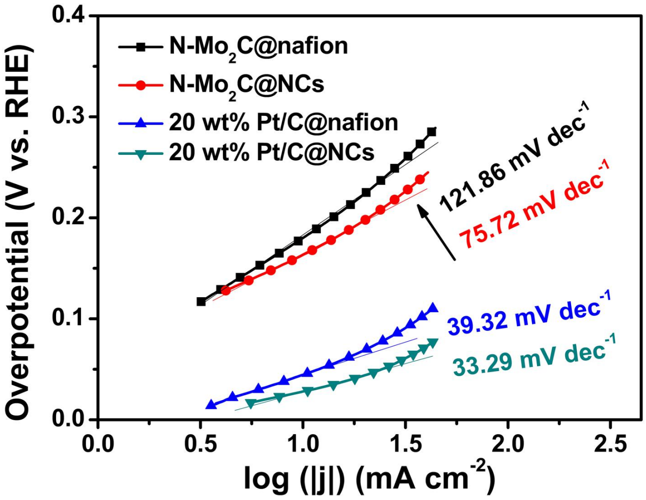

Figure S10. Tafel plots derived from **Figure 2B**, related to **Figure 2**.

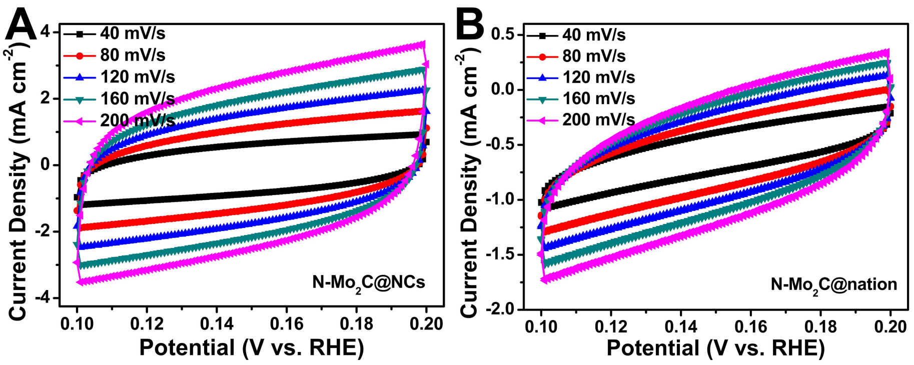

Figure S11. Cyclic voltammograms (CVs) curves of (A) N-Mo_2C@NCs and (B) N-Mo_2C@nafion with different rates from 40 to 200 mV s^{-1} in 0.5 M H_2SO_4 electrolyte, related to **Figure 2**.

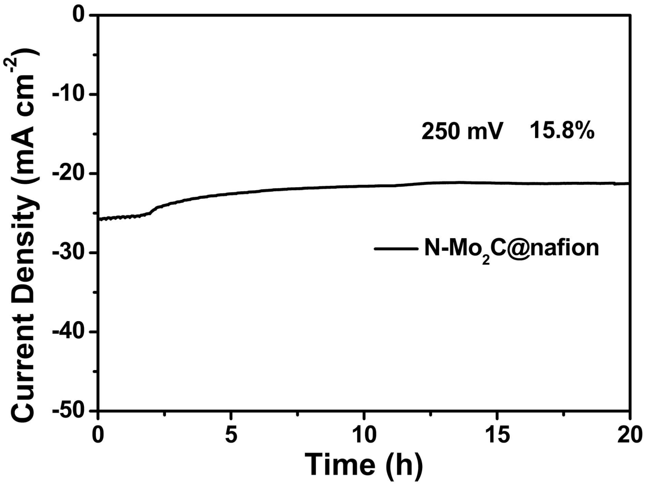

Figure S12. The chronoamperometry curve recorded at the overpotential of 250 mV driven from N-Mo_2C@nafion in 0.5 M H_2SO_4 solution, related to **Figure 2**.

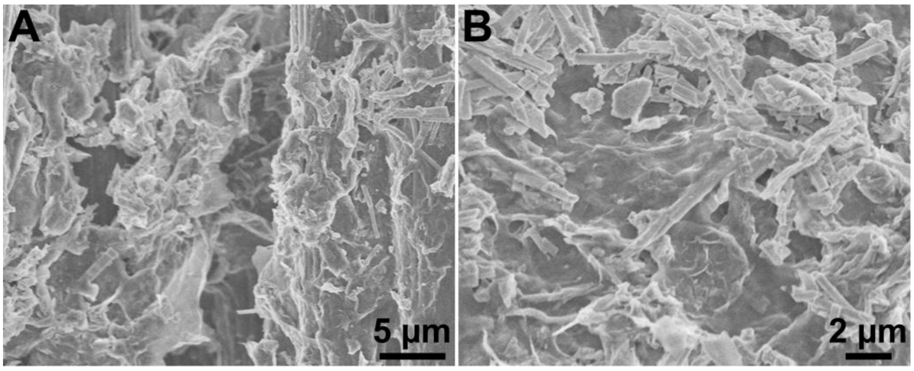

Figure S13. SEM images of N-Mo_2C@NCs loaded on carbon fibers, related to **Figure 2**.

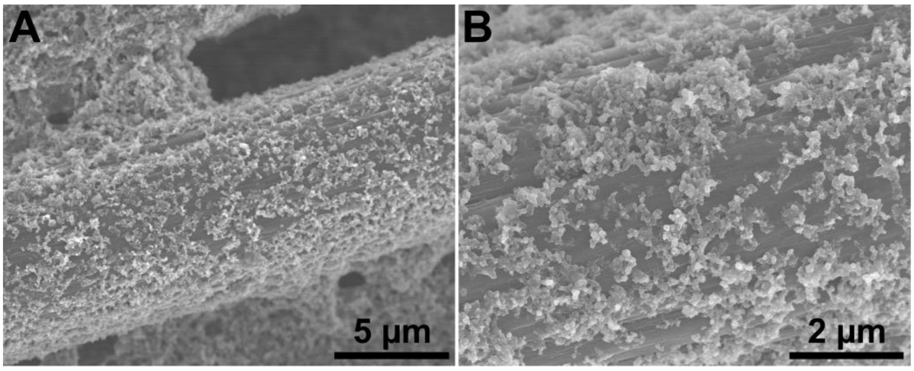

Figure S14. SEM images of 20 wt% Pt/C@NCs loaded on carbon fibers, related to

Figure 2.

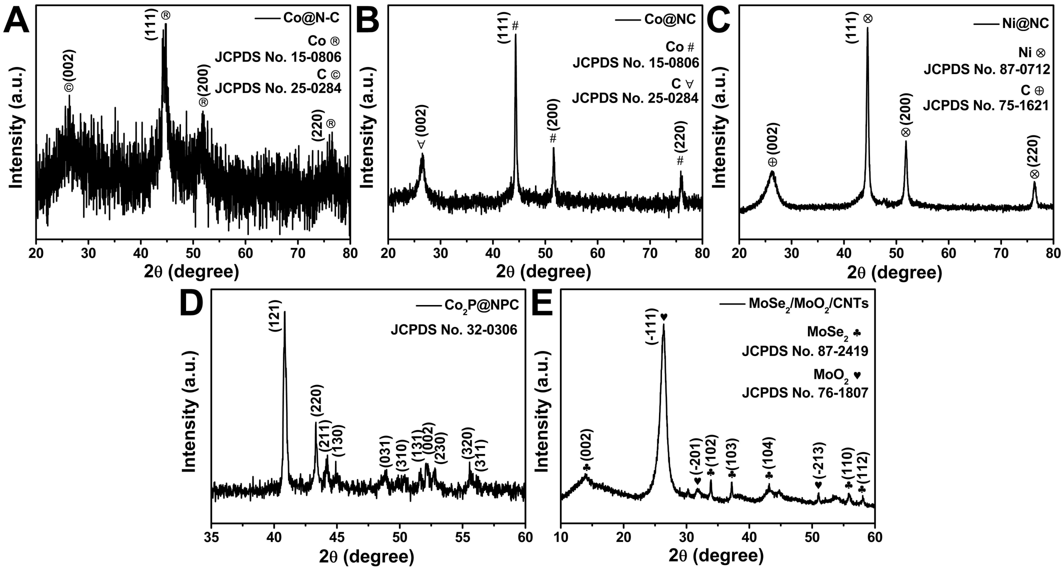

Figure S15. XRD patterns of as-prepared (A) Co@N-C, (B) Co@NC, (C) Ni@NC, (D) Co_2P@NPC, and (E) $MoSe_2$/MoO_2/CNTs catalysts, related to **Figure 2**.

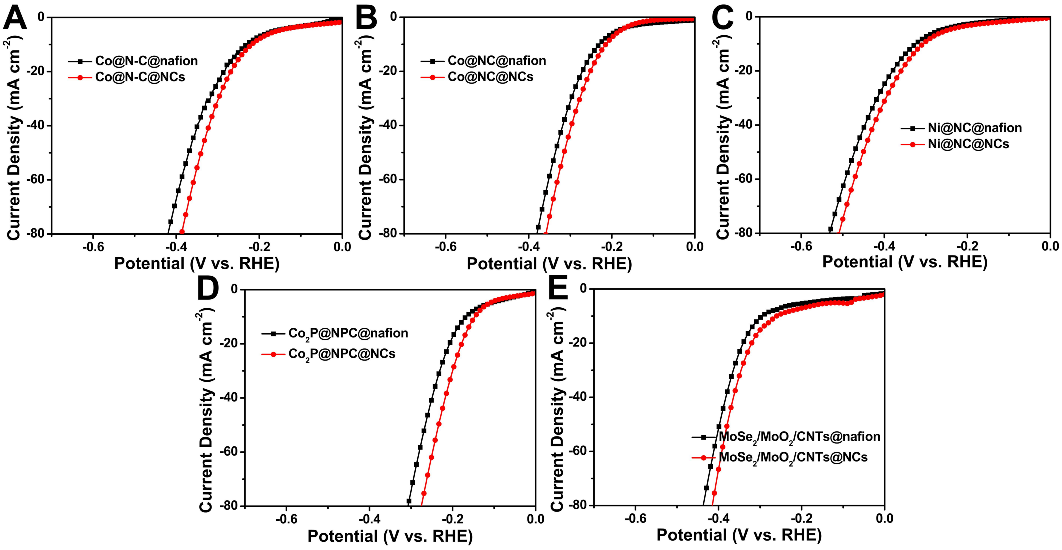

Figure S16. Polarization curves (without *iR* correction) of catalysts bonded with nafion and nanocellulose, respectively, including (A) Co@N-C, (B) Co@NC, (C) Ni@NC, (D) Co_2P@NPC, and (E) $MoSe_2$/MoO_2/CNTs, related to **Figure 2**.

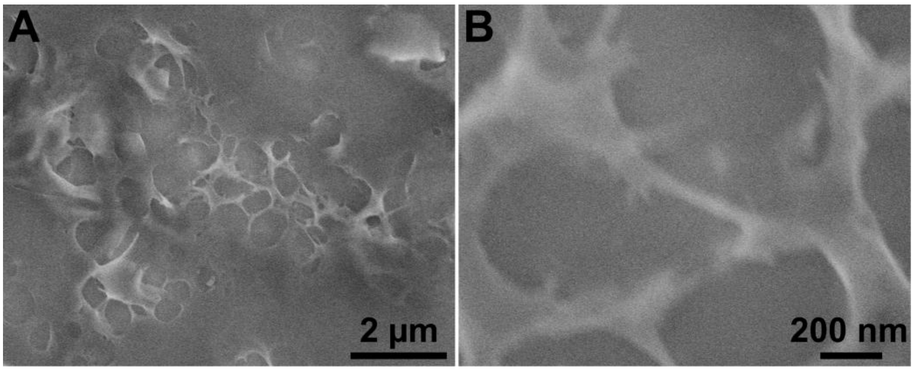

Figure S17. SEM images of pure nanocelluloses, related to **Figure 3**.

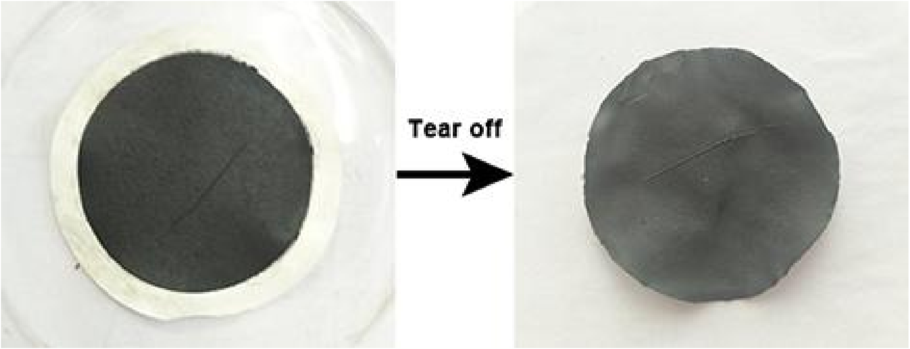

Figure S18. A physical film of N-Mo_2C@NCs was formed by suction filtration only using N-Mo_2C nanobelts and nanocellulose, related to **Figure 3**.

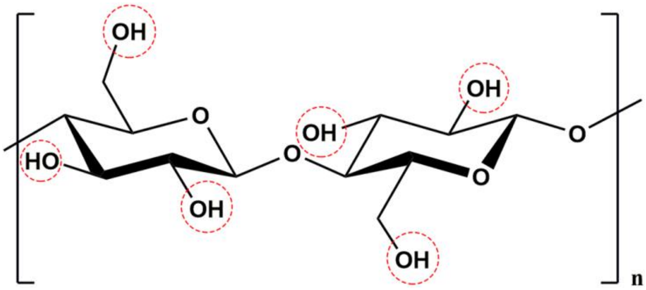

Figure S19. Molecular structure of nanocellulose, related to **Figure 3**.

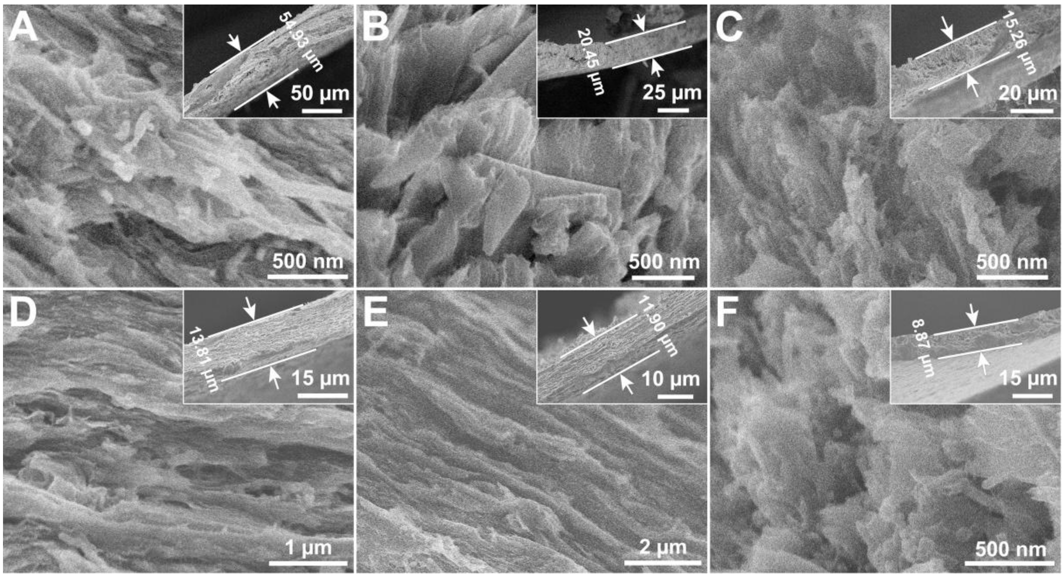

Figure S20. SEM images (A-F) with cross-sectional view of N-Mo_2C/G@NCs films with different thicknesses, related to **Figure 3**.

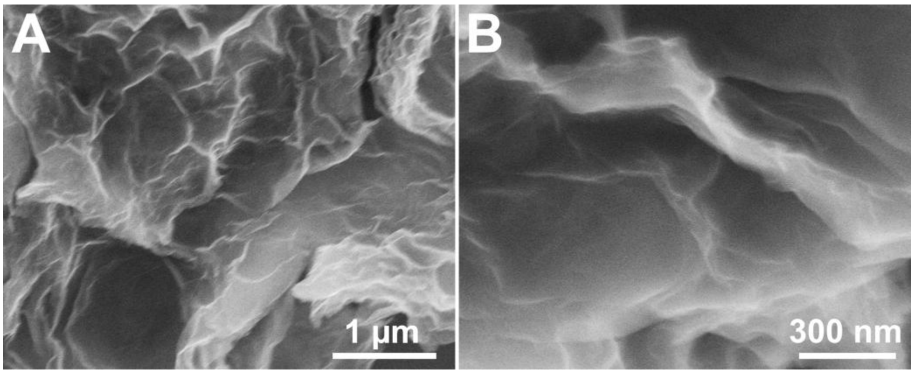

Figure S21. SEM images of graphene nanosheets, related to **Figure 3**.

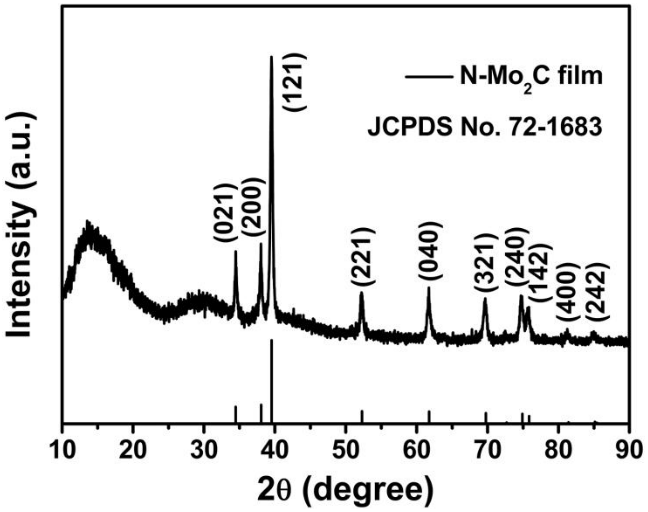

Figure S22. XRD result of N-Mo_2C/G@NCs, related to **Figure 3**.

It could be seen from **Figure S22** that XRD confirmed the prepared flexible films were composed of Mo_2C with characteristic peaks at 34.47° (021), 38.07° (200), 39.53° (121), 52.29° (221), 61.76° (040), 69.77° (321), 74.90° (240), 75.85° (142), 81.42° (400), and 85.12° (242), and the crystalline carbon with characteristic peaks at about 15° and 30°, which was consistent with the crystalline phase of N-Mo_2C powder.

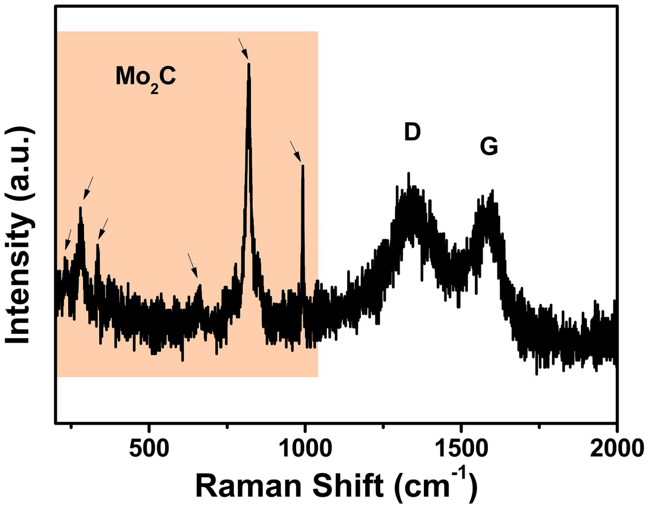

Figure S23. Raman result of N-Mo_2C/G@NCs, related to **Figure 3**.

In **Figure S23**, the N-Mo_2C/G@NCs composite film was further characterized by Raman spectroscopy, which exhibited two distinct peaks located at around 1343 and 1575 cm^{-1}, attributed to the D-band and G-band of the carbon-based matrix, respectively (Lin et al., 2016). And the film was accompanied by an I_D/I_G value of 1.09, indicating a large amount of disordered carbon existing in the carbon shell drived from N-doped Mo_2C. In addition, it could be observed from **Figure S23** was the presence of Mo_2C, which could further support the successful preparation of N-Mo_2C/G@NCs (Xiao et al., 2014).

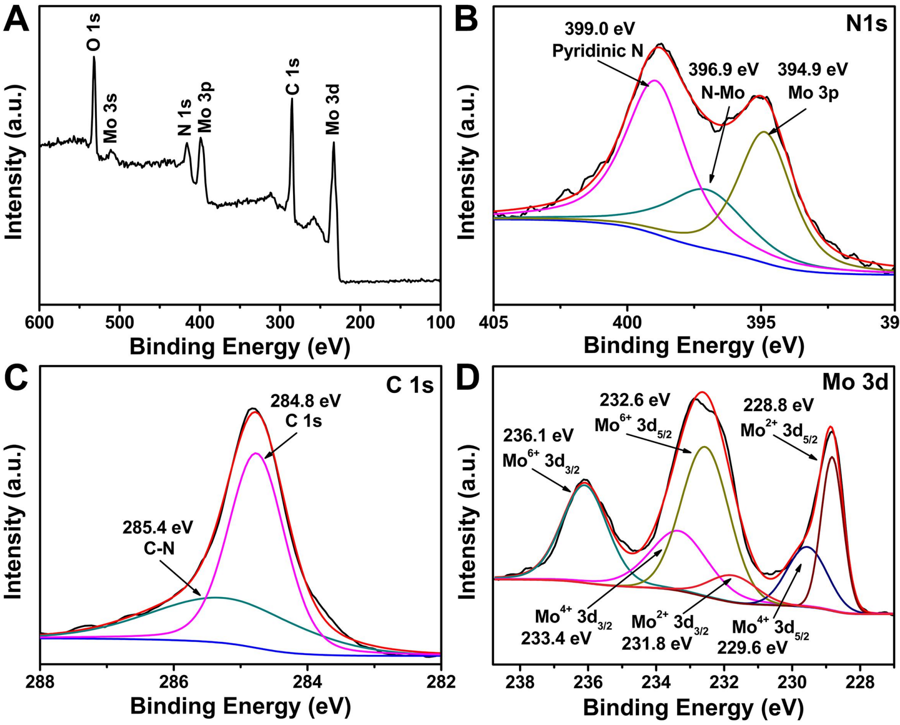

Figure S24. XPS spectra of (A) survey spectrum, (B) N 1s, (C) C 1s, and (D) Mo 3d for N-Mo_2C/G@NCs, related to **Figure 3**.

We accordingly studied the composition of N-Mo_2C nanobelt with X-ray photoelectron spectroscopy (XPS) analysis. As shown in **Figure S24A**, the survey spectra confirmed the presence of C, N, and Mo elements in N-Mo_2C sample. The C 1s, N 1s, and Mo 3d XPS spectra of N-Mo_2C were deconvoluted to estimate the relative contributions of C, N, and Mo species. As illustrated in **Figure S24B**, the N 1s XPS spectrum peak located at 399.0 eV was attributed to pyridinic-N, whereas the peak at 396.9 eV was associated with the N-Mo bonding state (Huang et al., 2018;

Huang et al., 2016). Especially, pyridinic-N exhibited the highest peak in this work and it has been proven to be beneficial for enhancing the electrocatalytic performance of water splitting (Lai et al., 2012). The C 1s peak could be deconvoluted into two peaks centered at 284.8 and 285.4 eV, arising from C-C and C-N, respectively (**Figure S24C**) (Li et al., 2018). Peak deconvolution of Mo 3d verified the existence of Mo_2C (Mo^{2+} $3d_{5/2}$ at 228.8 eV and Mo^{2+} $3d_{3/2}$ at 231.8 eV), MoO_2 (Mo^{4+} $3d_{5/2}$ at 229.6 eV and Mo^{4+} $3d_{3/2}$ at 233.4 eV), and MoO_3 (Mo^{6+} $3d_{5/2}$ at 232.6 eV and Mo^{6+} $3d_{3/2}$ at 236.1 eV), as shown in **Figure S24D** (Wan et al., 2014; Wu et al., 2016). The presence of a significant amount of superficial oxides was not surprising, which seemed to be inevitable due to the surface oxidation of N-Mo_2C nanobelt exposed to air (Huang et al., 2016; Jiang et al., 2017).

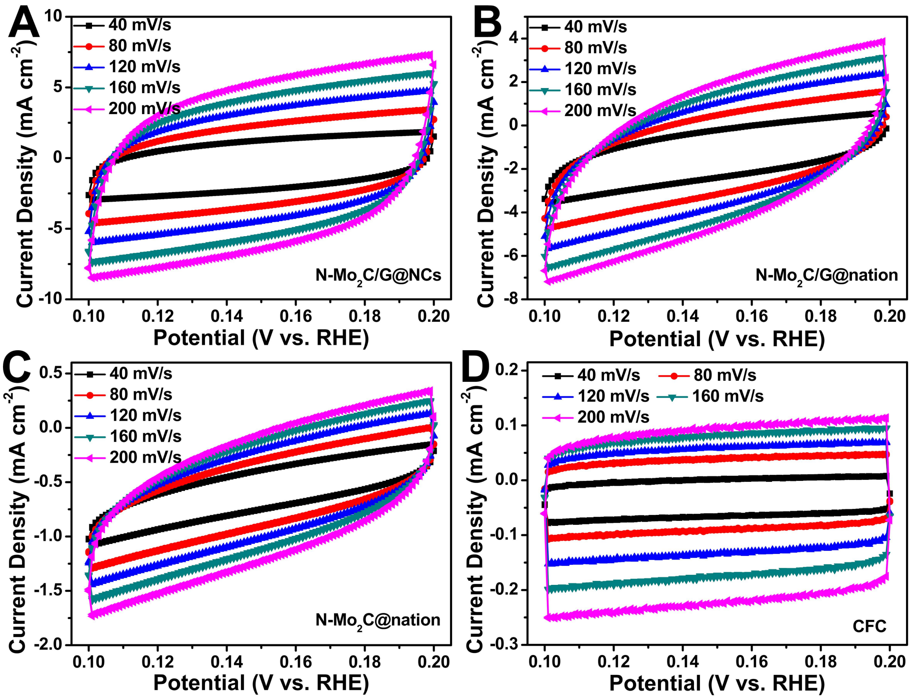

Figure S25. CVs curves of (A) N-Mo_2C/G@NCs, (B) N-Mo_2C/G@nafion, (C) N-Mo_2C@nafion, and (D) bare CFC with different rates from 40 to 200 mV s^{-1} in 0.5 M H_2SO_4 electrolyte, related to **Figure 4**.

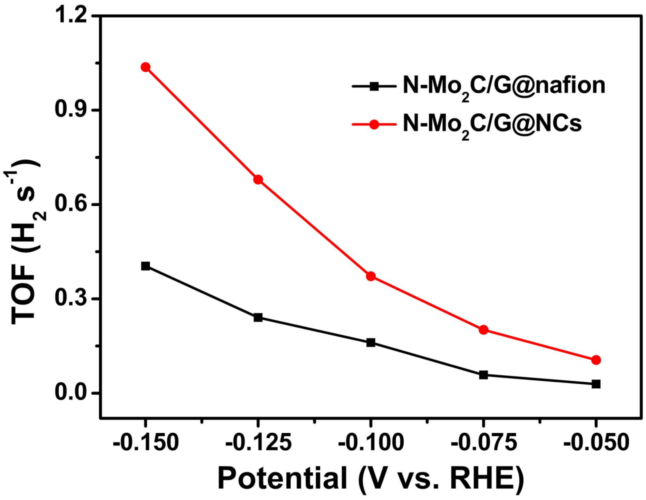

Figure S26. The TOF values plotted against the potential of N-Mo_2C/G@NCs and N-Mo_2C/G@nafion, related to **Figure 4**.

Assuming that all of active sites were entirely accessible to the electrolyte, the TOF values were calculated and plotted against the potential.

The following formula was used to calculate TOF:

$$\mathrm{TOF} = \frac{I}{2Fn}$$

where F and n are the Faraday constant and the number of active sites, respectively; I is the current density of LSV curves.

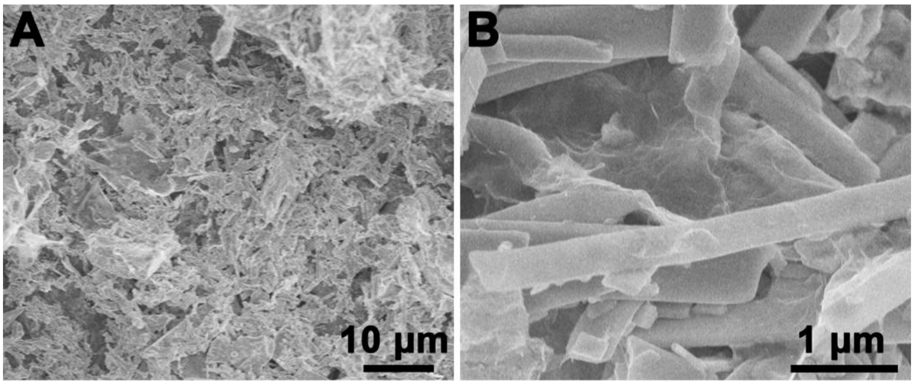

Figure S27. SEM images of N-Mo_2C/G@NCs after i-t testing, related to **Figure 4**.

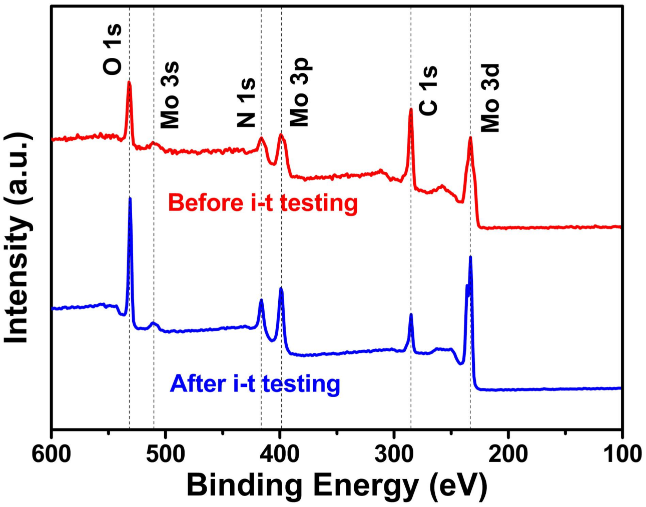

Figure S28. XPS survey spectra for N-Mo_2C/G@NCs before and after the i-t testing, related to **Figure 4**.

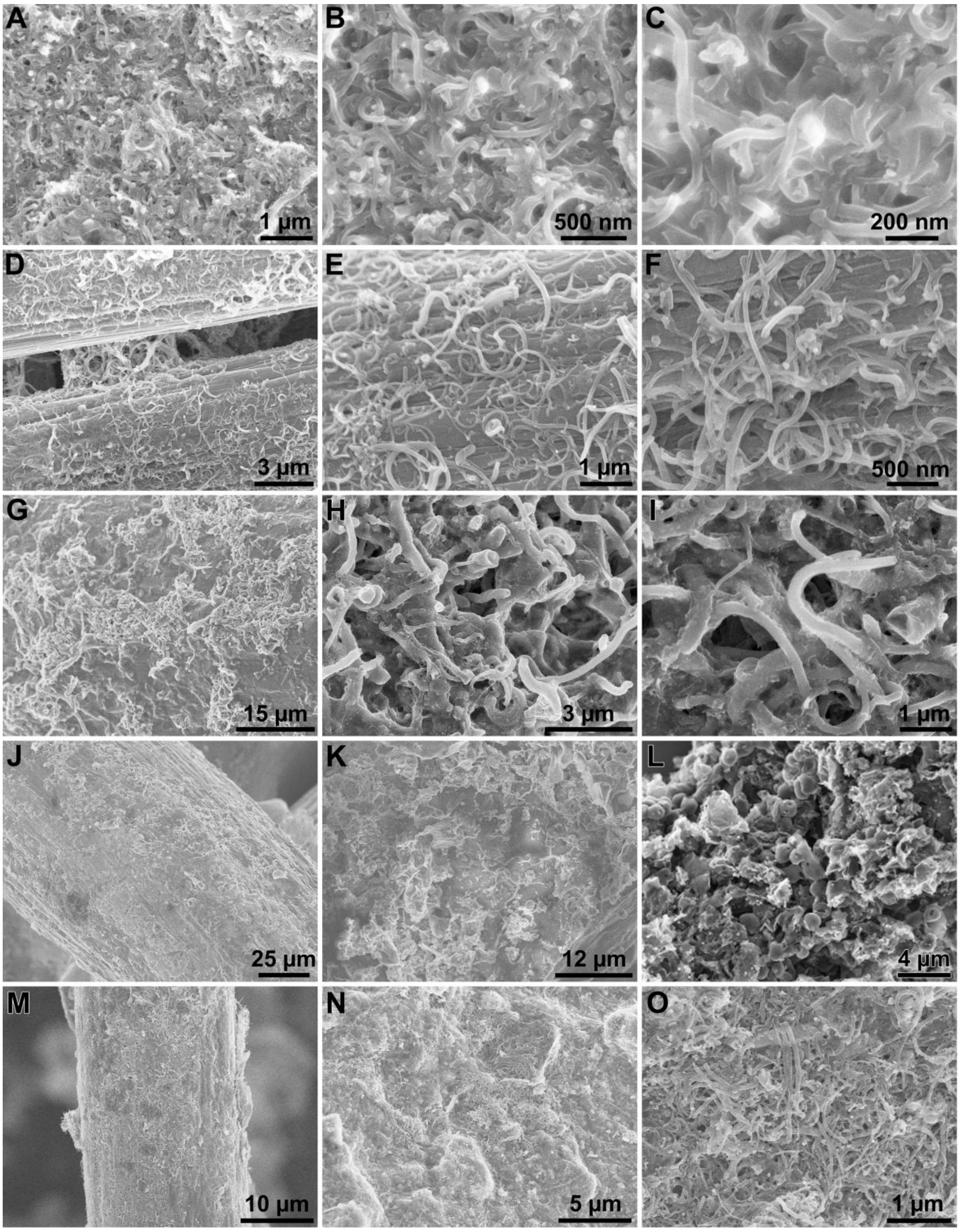

Figure S29. SEM images of (A-C) Co@N-C/G@NCs, (D-F) Co@NC/G@NCs, (G-I) Ni@NC/G@NCs, (J-L) Co_2P@NPC/G@NCs, and (M-O) $MoSe_2$/MoO_2/CNTs/G@NCs loaded on carbon fibers, related to **Figure 4**.

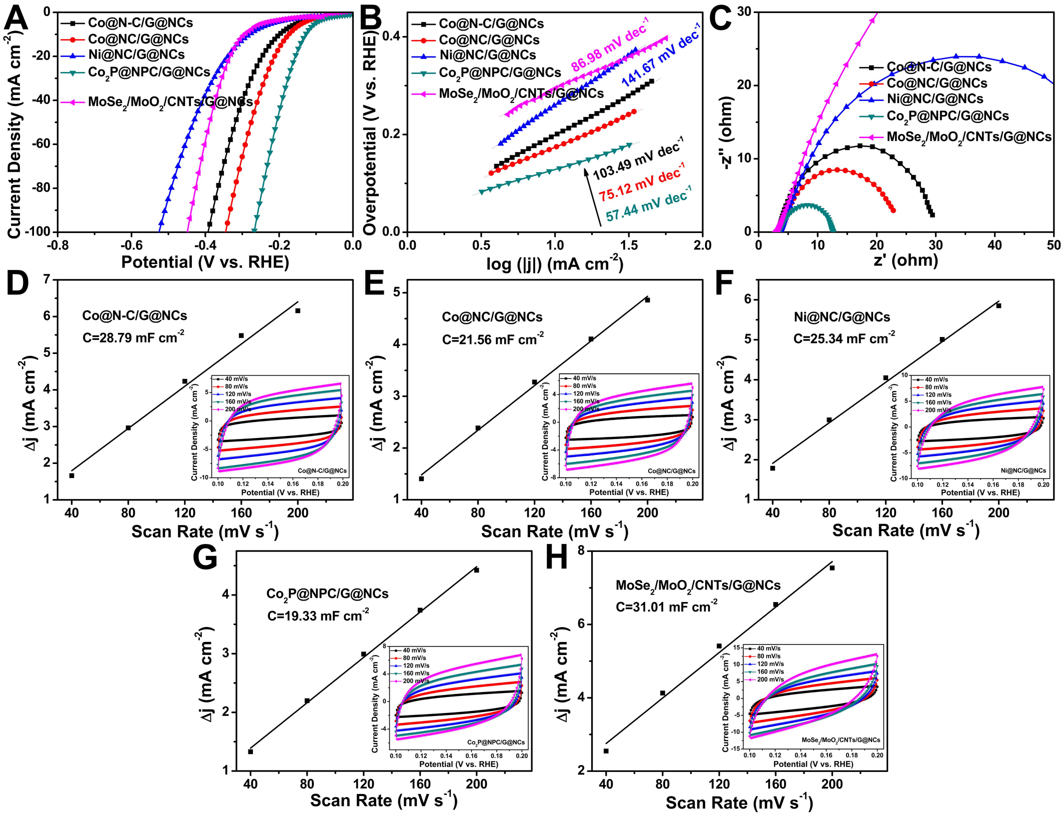

Figure S30. Polarization curves without *iR* correction (A), Tafel plots (B), EIS Nyquist plots (C) of the synthesized Co@N-C/G@NCs, Co@NC/G@NCs, Ni@NC/G@NCs, Co_2P@NPC/G@NCs, and $MoSe_2/MoO_2$/CNTs/G@NCs. The electrical double-layer capacitance and corresponding CVs curves of (D) Co@N-C/G@NCs, (E) Co@NC/G@NCs, (F) Ni@NC/G@NCs, (G) Co_2P@NPC/G@NCs, and (H) $MoSe_2/MoO_2$/CNTs/G@NCs. Related to **Figure 4**.

Transparent Methods

Materials

Mo powder (Mo) and hydrogen peroxide (H_2O_2, 30% w/w) were provided by Aladdin. Dicyandiamide ($C_2H_4N_4$, 99.99%) was obtained from Shanghai Macklin Biochemical Co., Ltd. Graphene (1 mg mL^{-1}) was offered by Nanjing XFNANO Materials Tech Co., Ltd. Nanocellulose dispersion (1%) was purchased from Anhui Sunvo Medicinal Materials Co., Ltd (Hefei, China). And ethanol absolute (EtOH, CH_3CH_2OH) was purchased from Guangdong Guanghua Sci-Tech Co., Ltd., China. Commercial Pt/C (20 wt%) catalyst was kindly supplied by Alfa Aesar. Nafion solution (~5% in a mixture of lower aliphatic alcohols and water) was purchased from Sigma-Aldrich Shanghai Co., and sulfuric acid (H_2SO_4) was obtained from Sinopharm Chemical Reagent Co. The carbon fiber cloth (CFC) was purchased from CeTech Co., Ltd., China. Argon (Ar) was obtained from Guangzhou YIGAS Gases Co., Ltd., China. Deionized (D.I.) water was supplied with a Barnstead Nanopure Water System (18.2 MΩ·cm) and used throughout the experiment.

Synthesis of Molybdenum Oxide Nanobelts (MoO_3 NBs).

In our experiments, molybdenum oxide nanobelts (MoO_3 NBs) as a precursor were prepared following a reported method (Zheng et al., 2009; Yang et al., 2018). In a typical procedure, 1.2 g pure Mo powder was slowly added into a beaker, which contained 10 mL of H_2O_2 aqueous solution (30 wt%). And then it was stirred vigorously for 1 h in an ice-water bath. Soon after, a transparent and yellow solution was formed, containing the water-soluble precursor of $MoO_2(OH)(OOH)$ (Zheng et al., 2009). Furthermore, 62.5 mL of D.I. water was added into the above solution under magnetic stirring for 6 h, and then a homogeneous aqueous solution was formed. Subsequently, the obtained solution was transferred into a Teflon-lined stainless steel autoclave with a volume of 100 mL, which was hydrothermally treated at 220 °C for 48 h. After the temperature was lowered to room temperature, the mixture was centrifuged to obtain an off-white product of MoO_3 NBs, Finally, the MoO_3 NBs precursor was washed with D.I. water three times, and then dried at 60 °C for 12 h in a vacuum oven.

Synthesis of Nitrogen-doped Molybdenum Carbide Nanobelts (N-Mo_2C NBs).

200 mg of commercial dicyandiamide powders ($C_2H_4N_4$) and 100 mg of obtained MoO_3 NBs were mixed in a ceramic boat and then were sealed, which was placed in a tube furnace with Ar gas to remove air. After that, the mixture was calcined at 450 °C for 2 h and then 800 °C for 2 h to form nitrogen-doped molybdenum carbide nanobelt (N-Mo_2C NBs).

Preparation of the Composite Film of Nitrogen-doped Molybdenum Carbide Nanobelts/Graphene Nanosheets Bonded with Nanocelluloses (N-Mo_2C/G@NCs film).

2 mL of nanocellulose dispersion (1%), 1 mL of graphene (1 mg mL^{-1}) and 1 mL of ethanol absolute were added to a 10 mL glass vials. The weighed 20 mg of synthesized N-Mo_2C NBs powder was transferred to the above glass bottle. The mixture was then placed in an ultrasonic instrument for 30 min to obtain a homogeneously mixed solution. Subsequently, the resulting solution was filtrated dropwise through a filter membrane (pore size of 0.22 μm). Finally, the free-standing flexible and porous N-Mo_2C/G@NCs film could be obtained after drying at room temperature, peeled off from the filter membrane.

In the similar way, the slurry of N-Mo_2C@nafion and N-Mo_2C/G@nafion was obtained. In addition, after undergoing sonication, the mixed solution could be taken out and dropped onto the carbon fiber cloth, which was dried at room temperature to abtain N-Mo_2C@nafion loaded on carbon nanofiber cloth (N-Mo_2C@nafion/CFC), which was used as electrode because N-Mo_2C@nafion could not form a film by itself. In the similar manner, N-Mo_2C/G@nafion/CFC was also obtained.

Preparation and Film Formation of Other Powder Catalysts

According to the reported literatures, five other powder catalysts were synthesized. Cobalt nanoparticles encapsulated in nitrogen-doped carbon nanotubes (Co@N-C) was obtained by a simple pyrolysis of Co-MOF (ZIF-67) (Yu et al., 2018). Nitrogen-doped carbon nanotube-coated cobalt nanoparticles (Co@NC) and nitrogen-doped carbon nanotube-coated nickel nanoparticles (Ni@NC) were prepared by pyrolysis of cobalt salt and nickel salt with dicyandiamide, respectively (Zou et al., 2014; Zhou et al., 2016). The Co_2P nanoparticles embedded into N, P co-doped carbon shells (Co_2P@NPC) was synthesized by high temperature *in situ* phosphating of Co^{2+}/*saccharomycetes* derived from cobalt ions adsorbed *saccharomycete* cells (Li et al., 2018). $MoSe_2$ nanosheet/MoO_2 nanobelt/carbon nanotube ($MoSe_2$/MoO_2/CNTs) was composed of highly conductive CNTs and hierarchical $MoSe_2$ nanosheets ($MoSe_2$ NSs) on MoO_2 nanobelts (MoO_2 NBs), respectively (Yang et al., 2018). In this part, MoO_2 NBs was obtained from the thermal reduction of MoO_3 NBs and $MoSe_2$ NSs was obtained from the thermal selenization of MoO_2 NBs.

Similarly, as-prepared Co@N-C, Co@NC, Ni@NC, Co_2P@NPC, and $MoSe_2$/MoO_2/CNTs, in the form of powders, were also used to prepare Co@N-C/G@NCs, Co@NC/G@NCs, Ni@NC/G@NCs, Co_2P@NPC/G@NCs, and $MoSe_2$/MoO_2/CNTs/G@NCs films supported on CFC using the similar procedure to the above.

Characterizations

Phase compositions of the as-made materials were measured by D8 Advance (Germany Bruker) X-ray diffraction (XRD) patterns using Cu Kα radiation ($\lambda = 0.15406$ nm) at a scanning rate of 0.02°/s in the range of $10° < 2\theta < 90°$. Raman spectra were got by a LabRAM HR800 spectrometer (Horiba Jobin Yvon, FR.) equipped with a Diode Pump Solid State Laser (wavelength =532 nm). Morphologies of the materials were identified by a field emission scanning electron microscopy (FESEM, MERLIN Compact, Carl Zeiss) and a transmission electron microscopy (TEM, a JEM-2100F Field Emission Electron Microscope, JPN) at an acceleration voltage of 200 kV. X-ray photoelectron spectroscopy (XPS) measurement was carried out on a PHI X-tool instrument (Ulvac-Phi). Brunauer-Emmet-Teller (BET) specific surface area and pore size distribution were attained on a Quantachrome Autosorb-IQ$_2$ instrument with nitrogen adsorption at 77 K using the Barrett-Joyner-Halenda (BJH) method. The thicknesses of MoO_3 NBs and N-Mo_2C NBs were analyzed by means of atomic force microscopy (AFM, BRUKER Dimension Icon with ScanAsyst, Santa Barbara, USA), operated at room temperature and ambient conditions.

Electrochemical Measurements

All the electrochemical measurements were performed with an electrochemical workstation (CHI 760C, CH Instruments Inc.) in 0.5 M H_2SO_4 aqueous solution using a three-electrode configuration. An Ag/AgCl electrode (SCE, saturated KCl) and carbon rod were used as the reference and counter electrode, respectively. The amount of nafion and nanocellulose were 50 μL nafion/5 mg N-Mo_2C and 500 μL nanocellulose dispersion (1%)/5 mg N-Mo_2C, respectively, when comparing their properties. In order to compare the properties of nafion bonded and nanocellulose bonded catalysts, and to highlight the advantages of film forming components, while avoiding the effects of non-filming comparative samples during the test (no added nanocellulose), such as N- Mo_2C@nafion and N-Mo_2C/G@nafion, electrochemical tests of non-filming samples were carried out by loading the slurry onto carbon fiber cloth as working electrodes. Polarization curves were achieved by sweeping the potential from 0 to −0.5 V vs. RHE at a potential sweep rate of 5 mV s^{-1}. AC impedance was detected with a frequency range and an amplitude of 10 mV from 0.01 Hz to 100 kHz. The main arc in electrochemical impedance spectroscopy (EIS) spectra was matched utilising a simplified Randles equivalent circuit, which was comprised of a resistance (R_s) in series with a parallel arrangement of a charge-transfer resistance (R_{ct}) and a constant phase element (CPE), and the fitting parameters were appraised through the Levenberg-Marquardt minimization procedure. The electrochemical double layer capacitance was probed by Cyclic voltammetry (CV) at nonfaradaic potentials as another way to reckon the efficient electrochemical active area of HER. Current-time responses were monitored by chronoamperometric measurements by three fixed overpotentials of 286 mV for 100 h, 394 mV for 77 h, and 492 mV for 60 h, respectively. In all electrochemical measurements, the potential of reference electrode was calibrated with respect to a reversible hydrogen electrode (RHE), which was performed in a high-purity H_2 (99.999%) saturated electrolyte with a Pt wire as the working electrode and counter electrode. And then cyclic voltammograms (CVs) were collected at a scan rate of 2 mV s^{-1}, and the average of the two potentials at which the current crossed zero was taken as the thermodynamic potential for the hydrogen electrode reactions. Then in 0.5 M H_2SO_4, it was available that E(SCE) = E(RHE) + (–0.267 V), as shown in **Figure S9**.

Supplemental References

Huang, Y., Ge, J., Hu, J., Zhang, J., Hao, J., Wei, Y. (2018). Nitrogen-Doped Porous Molybdenum Carbide and Phosphide Hybrids on a Carbon Matrix as Highly Effective Electrocatalysts for the Hydrogen Evolution Reaction. *Adv. Energy Mater. 8*, 1701601;

Huang, Y., Gong, Q., Song, X., Feng, K., Nie, K., Zhao, F., Wang, Y., Zeng, M., Zhong, J., Li, Y. (2016). Mo_2C Nanoparticles Dispersed on Hierarchical Carbon Microflowers for Efficient Electrocatalytic Hydrogen Evolution. *ACS Nano 10*, 11337-11343.

Jiang, J., Liu, Q., Zeng, C., Ai, L. (2017). Cobalt/molybdenum carbide@ N-doped carbon as a bifunctional electrocatalyst for hydrogen and oxygen evolution reactions. *J. Mater. Chem. A 5*, 16929-16935.

Lai, L., Potts, J. R., Zhan, D., Wang, L., Poh, C. K., Tang, C., Gong, H., Shen, Z., Lin, J., Ruoff, R. S. (2012). Exploration of the active center structure of nitrogen-doped graphene-based catalysts for oxygen reduction reaction. *Energy Environ. Sci. 5*, 7936-7942.

Li, G., Yu, J., Jia, J., Yang, L., Zhao, L., Zhou, W., Liu, H. (2018). Cobalt–Cobalt Phosphide Nanoparticles@Nitrogen-Phosphorus Doped Carbon/Graphene Derived from Cobalt Ions Adsorbed Saccharomycete Yeasts as an Efficient, Stable, and Large-Current-Density Electrode for Hydrogen Evolution Reactions. *Adv. Funct. Mater. 28*, 1801332.

Lin, H., Liu, N., Shi, Z., Guo, Y., Tang, Y., Gao, Q. (2016). Cobalt-Doping in Molybdenum-Carbide Nanowires Toward Efficient Electrocatalytic Hydrogen Evolution. *Adv. Funct. Mater. 26*, 5590-5598.

Wan, C., Regmi, Y. N., Leonard, B. M. (2014). Multiple phases of molybdenum carbide as electrocatalysts for the hydrogen evolution reaction. *Angew. Chem. Int. Ed. 126*, 6525-6528;

Wu, Z.-Y., Hu, B.-C., Wu, P., Liang, H.-W., Yu, Z.-L., Lin, Y., Zheng, Y.-R., Li, Z., Yu, S.-H. (2016). Mo_2C nanoparticles embedded within bacterial cellulose-derived 3D N-doped carbon nanofiber networks for efficient hydrogen evolution. *NPG Asia Mater. 8*, e288.

Xiao, P., Yan, Y., Ge, X., Liu, Z., Wang, J. Y., Wang, X. (2014). Investigation of molybdenum carbide nano-rod as an efficient and durable electrocatalyst for hydrogen evolution in acidic and alkaline media. *Appl. Catal. B: Environ. 154*, 232-237.

Yang, L., Deng, Y., Zhang, X., Liu, H., Zhou, W. (2018). $MoSe_2$ nanosheet/MoO_2 nanobelt/carbon nanotube membrane as flexible and multifunctional electrodes for full water splitting in acidic electrolyte. *Nanoscale 10*, 9268-9275.

Yu, J., Li, G., Liu, H., Wang, A., Yang, L., Zhou, W., Hu, Y., Chu, B. (2018). Simultaneous water recovery and hydrogen production by bifunctional electrocatalyst of nitrogen-doped carbon nanotubes protected cobalt nanoparticles. *Int. J. Hydrogen Energy 43*, 12110-12118.

Zheng, L., Xu, Y., Jin, D., Xie, Y. (2009). Novel Metastable Hexagonal MoO_3 Nanobelts: Synthesis, Photochromic, and Electrochromic Properties. *Chem. Mater. 21*, 5681-5690;

Zhou, W., Lu, J., Zhou, K., Yang, L., Ke, Y., Tang, Z., Chen, S. (2016). $CoSe_2$ nanoparticles embedded defective carbon nanotubes derived from MOFs as efficient electrocatalyst for hydrogen evolution reaction. *Nano Energy 28*, 143-150.

Zou, X., Huang, X., Goswami, A., Silva, R., Sathe, B. R., Mikmeková, E., Asefa, T. (2014). Cobalt-embedded nitrogen-rich carbon nanotubes efficiently catalyze hydrogen evolution reaction at all pH values. *Angew. Chem. Int. Ed. 53*, 4372-4376;